AD-A254 772
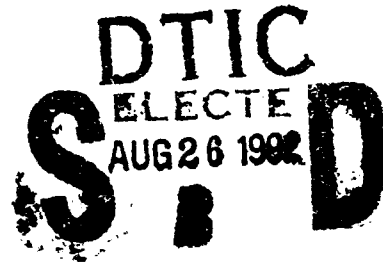
RL-TR-92-92
Final Technical Report
May 1992

TERAHERTZ HORN ANTENNAS ON THIN MEMBRANES

California Institute of Technology

DTIC
ELECTE
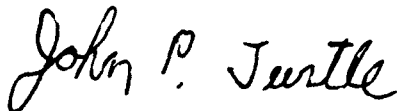AUG 26 1992
S D

404888

92-23610

Rome Laboratory
Air Force Systems Command
Griffiss Air Force Base, NY 13441-5700

92 8 25 044

This report has been reviewed by the Rome Laboratory Public Affairs Office (PA) and is releasable to the National Technical Information Service (NTIS). At NTIS it will be releasable to the general public, including foreign nations.

RL-TR-92-92 has been reviewed and is approved for publication.

APPROVED: *John P. Turtle*

JOHN P. TURTLE
Project Engineer

FOR THE COMMANDER: *John K. Schindler*

JOHN K. SCHINDLER
Director
Electromagnetics & Reliability Directorate

TERAHERTZ HORN ANTENNAS ON THIN MEMBRANES

David Rutledge

Contractor: California Institute of Technology
Contract Number: F19628-87-K-0051
Effective Date of Contract: 04 September 1987
Contract Expiration Date: 31 October 1991
Short Title of Work: Terahertz Antennas
Period of Work Covered: Sep 87 - Oct 91

Principal Investigator: David Rutledge
               Phone: (818) 356-4806

RL Project Engineer: John P. Turtle
               Phone: (617) 377-2051

REPORT DOCUMENTATION PAGE

Form Approved
OMB No. 0704-0188

1. AGENCY USE ONLY (Leave Blank)	2. REPORT DATE May 1992	3. REPORT TYPE AND DATES COVERED Final Sep 87 - Oct 91

4. TITLE AND SUBTITLE
TERAHERTZ HORN ANTENNAS ON THIN MEMBRANES

5. FUNDING NUMBERS

C - F19628-87-K-0051
PE - 63218C
PR - S812
TA - C2
WU - 21

6. AUTHOR(S)

David Rutledge

7. PERFORMING ORGANIZATION NAME(S) AND ADDRESS(ES)
California Institute of Technology
Department of Electrical Engineering 116-81
Pasadena CA 91124

8. PERFORMING ORGANIZATION REPORT NUMBER

9. SPONSORING/MONITORING AGENCY NAME(S) AND ADDRESS(ES)
Strategic Defense Initiative   Rome Laboratory (ERAA)
Office, Office of the   Hanscom AFB MA 01731-5000
Secretary of Defense
Wash DC 20301-7100

10. SPONSORING/MONITORING AGENCY REPORT NUMBER

RL-TR-92-92

11. SUPPLEMENTARY NOTES

Rome Laboratory Project Engineer: John P. Turtle/ERAA(617) 377-2051

12a. DISTRIBUTION/AVAILABILITY STATEMENT
Approved for public release; distribution unlimited.

12b. DISTRIBUTION CODE

13. ABSTRACT (Maximum 200 words)

The Terahertz frequency range offers significant potential advantages for satellite systems. The use of miniature hollow metal waveguide at these high frequencies has made construction of such systems difficult and expensive. The goal of this program has been to apply integrated circuit fabrication techniques to increase flexibility and reliability, and to reduce cost. The focus of this effort has been the thin-membrane supported antenna in an etched horn. The horns are constructed in silicon using an anisotropic etch which naturally forms pyramidal holes. The antenna is supported within the horn on a membrane of silicon oxynitride, typically 1 m thick. Fabrication techniques have been developed for the production of individual horns, as well as linear and two-dimensional arrays for 93 and 242 GHz. Theoretical and measured patterns for the horns have been compared. A thin-film power-density meter has been designed. Imaging has been demonstrated at 93 GHz, using two-dimensional arrays.

14. SUBJECT TERMS
Integrated Circuit Antennas, Imaging Arrays, Terahertz

15. NUMBER OF PAGES
48

16. PRICE CODE

17. SECURITY CLASSIFICATION OF REPORT UNCLASSIFIED	18. SECURITY CLASSIFICATION OF THIS PAGE UNCLASSIFIED	19. SECURITY CLASSIFICATION OF ABSTRACT UNCLASSIFIED	20. LIMITATION OF ABSTRACT U/L

PUBLICATIONS

The key papers (appended) published under this contract are:

[1] Gabriel M. Rebeiz, Dayalan P. Kasilingam, Yong Guo, Philip A. Stimson, David B. Rutledge, "Monolithic Millimeter-Wave Two-Dimensional Horn Imaging Arrays," *IEEE Transactions on Antennas and Propagation, T-AP-38,*pp. 1473–1482, September 1990.

[2] Karen A. Lee, Yong Guo, Philip A. Stimson, Kent A. Potter, Jung-Chih Chiao, David B. Rutledge, "Thin-Film Power Density Meter for Millimeter Wavelengths," *IEEE Transactions on Antennas and Propagation, T-AP-39,* pp. 425–428, March 1991.

[3]Yong Guo, Karen Lee, Philip Stimson, Kent Potter, David Rutledge, "Aperature Efficiency of Integrated-Circuit Horn Antennas," *Mircrowave and Optical Technology Letters 4,* pp.6-9, January 5, 1991.

RESEARCH OVERVIEW

The terahertz frequency range offers significant potential advantages for satellite systems. These frequencies are strongly absorbed by the atmosphere, so there is no possibility of communications being intercepted by ground-based or airborne receivers. Terahertz systems would also achieve smaller antenna beamwidths than lower frequency microwave systems. The extention of microwave remote sensing methods to terahertz frequencies and the possibility of spectroscopic detection of rocket plumes is attractive. The use of miniature hollow metal waveguide at these high frequencies has made construction of such systems difficult and expensive.

Objectives:

The object of this program has been to apply integrated circuit fabrication techniques to increase flexibilty and reliability, and to reduce the cost of systems operating at these frequencies. The focus of this effort has been the thin-membrane supported antenna in an etched horn [1]. The horns are constructed in silicon using an anisotropic etch

which naturally forms pyramidal holes. The horns are built up using two or more silicon wafers, each containing a portion of the horns, as shown in Fig. 1, and in [1], Figs. 2 and 3. The antenna is supported within the horn on a membrane of silicon oxynitride, typically $1\,\mu$ m thick. This membrane is grown on the back side of one wafer using plasma enhanced chemical vapor deposition. Deposition parameters have been adjusted to produce membranes with low tensile stress. Higher tensile or any compressive stress results in membrane failure. Antennas and detectors are fabricated on the membrane using standard photolithographic techniques. Scale model measurements made at microwave frequencies (4–8 GHz) using an H/P 8510 vector network analyzer have been utilized to optimize the antenna structures. Theoretical patterns have been calculated for a single horn, assuming the horn to be part of an infinite two-dimensional array. Measured patterns at 93 and 242 GHz agree well with the calculated patterns.

Microbolometers have been used as detectors, as they can be calibrated to yield absolute power measurements. This is important in calculating the efficiency of the horn antennas. Difficulties arose in obtaining accurate measurements of the incident power density—also required for efficiency calculations. A thin-film power density meter was developed to overcome this difficulty [2]. The device consists of a thin-film bismuth bolometer vacuum deposited on mylar membrane. The incident radiation is partially absorbed by the bolometer, and is measurable as a change in resistance due to heating. Radiation not absorbed by the bolometer is trapped in a beam dump to avoid standing wave problems. The estimated accuracy of the power meter is 5% , which compares favorably with other available techniques. Using the power meter, loss mechanisms have been identified and eliminated to the extent possible. Horn antennna efficiency has been increased from an initial 44% to 72% as a result of this effort [3].

Imaging at 93 GHz has been demonstrated using a two-dimensional array of horn antennnas as a focal plane array. A fixed focal length lens, whose focal ratio was varied using aperature stops, was illuminated by plane wave radiation. System efficiency and power distribution in the focal plane (at the horn array) were measured as a function of focal ratio [1]. Results indicate that the horn array is well suited for diffraction limited imaging.

RECENT RESEARCH FINDINGS

Efforts have recently been directed toward improving the sensitivity of the horn arrays for imaging purposes. Two approaches have been taken. For broadband imaging, the antenna will feed a 90 GHz HEMT amplifier which in turn will drive the detector. For narrowband imaging, a double array of horns with integral mixers will be used. RF and LO power will be fed to separate arrays, on opposite faces of the stack of silicon wafers (Fig. 1). The current design uses a subharmonically pumped mixer. This reduces LO frequency, allowing the use of available mixer diode pairs. RF power will be summed from four square horns on the opposite side of the stack (Fig. 2). One trough-shaped horn will provide LO power for a mixer located between the loaded dipole probe at its center (Fig. 3). The use of four RF horns with one LO horn provides good geometric alignment which allows full utilization of the incident LO power. It should also sharpen the effective pattern of the RF horns, providing better coupling to systems with a more conservative focal ratio. The design for RF and LO probes, the interconnects, and a plot of measured impedance for a 9.5 GHz model is shown in Fig. 4. The impedance is that seen by the mixer. Measurements were again made using an H/P 8510 network analyzer. In the actual mixer array, the mixer diodes would be installed at the position indicated for the SMA connector in the figure. The RF match at 9.5 GHz leaves something to be desired, but involves a

trade-off between RF match, LO match, and RF–LO isolation. Extensive microwave model work indicates the compromise design, as shown, to be a good one.

The broadband imaging array design consists of individual horn elements similar to that shown in Fig. 5. By fabricating an array containing horn with and without the amplifier ahead of the detector, it should be possible to make a direct determination of the benefits of the amplifier. By using microbolometer detectors and the thin-film power density meter previously mentioned, absolute power and efficiency measurements can be made. The folded monopole (hairpin) probe shown in the figure is ideal from the standpoint of RF impedance matching. However, bias requirements for the amplifier preclude a DC path to ground in the input ciruit. Various probe configurations have been investigated using microwave models. In addition to the microwave models, the structure has been analyzed using the H/P High Frequency Structures Simulator, a finite element electromagnetics solver. Fig. 6 shows the field representation for the horn with a dipole probe and coplanar transmission line. Symmetry is invoked to split the horn, dipole, and line down the centerline to reduce computation time. The Smith Chart shows the impedance seen at the end of the coplanar line adjacent the horn wall. The microwave models seem to provide good results in substantially less time than the Structures Simulator.

FUTURE WORK

Recommended future work would include the fabrication of the mixer array and the broadband array. The latter would require additional effort in the area of probe design and/or biasing systems.
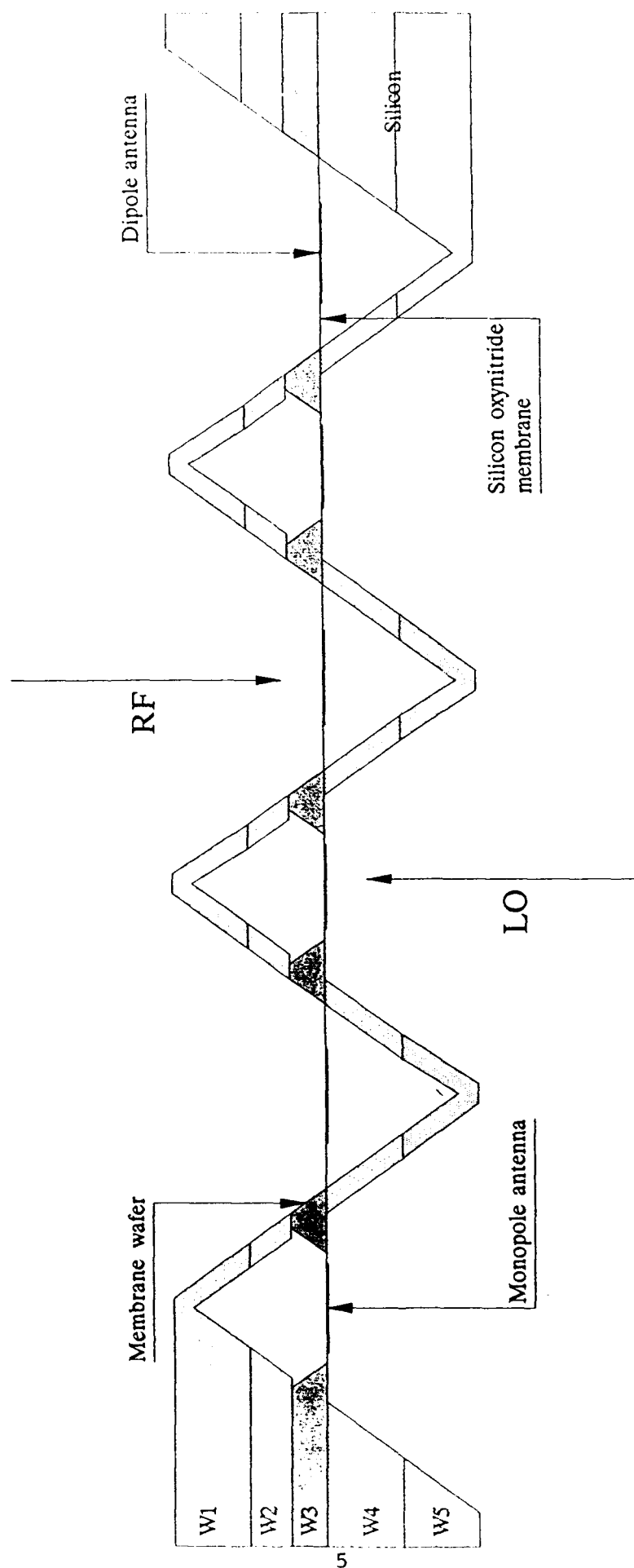
Figure 1. Monolithic Horn Array.

RF horn   Membrane   Monopole probe
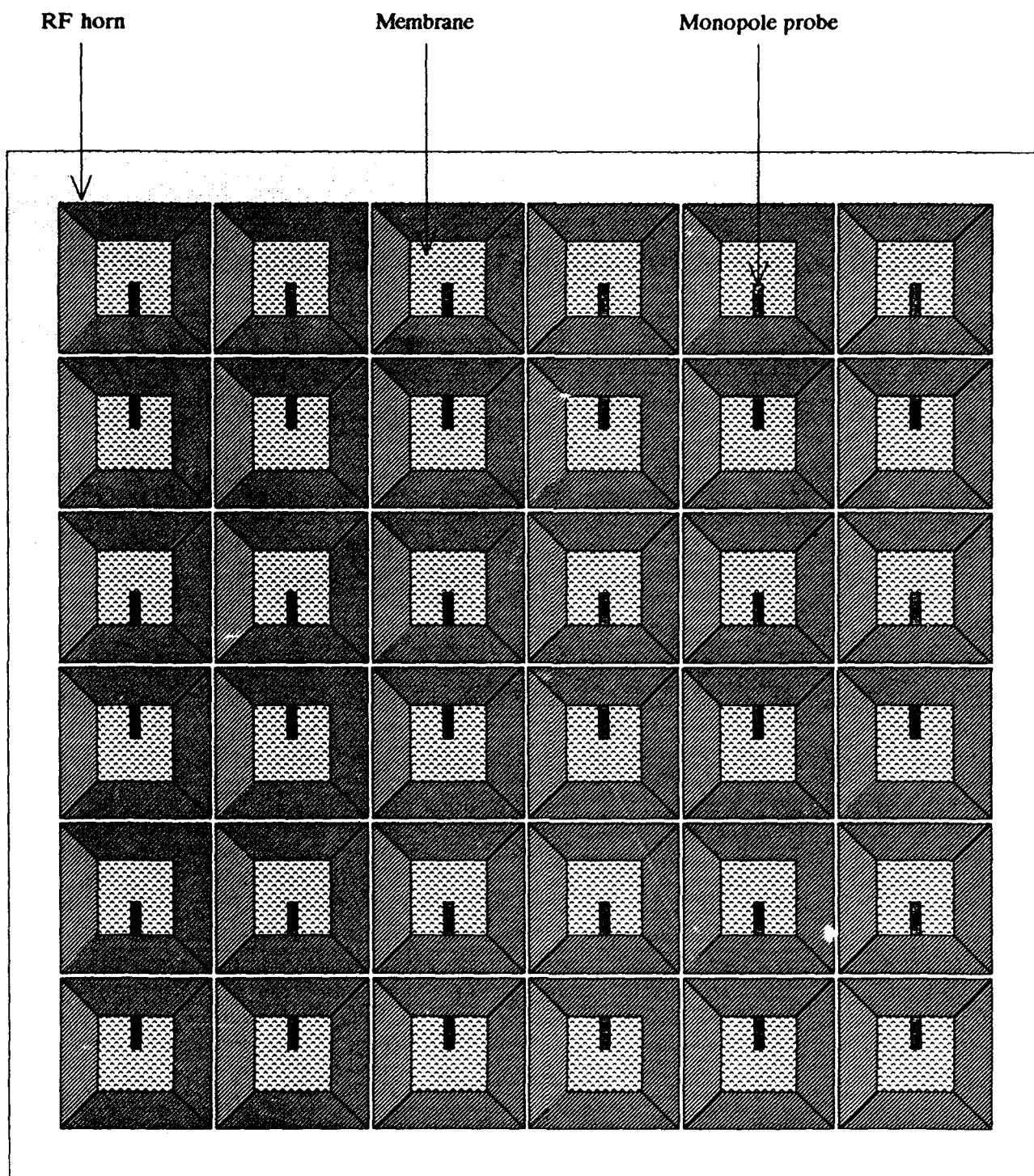
Figure 2. Proposed back-to-back horn array, RF face.
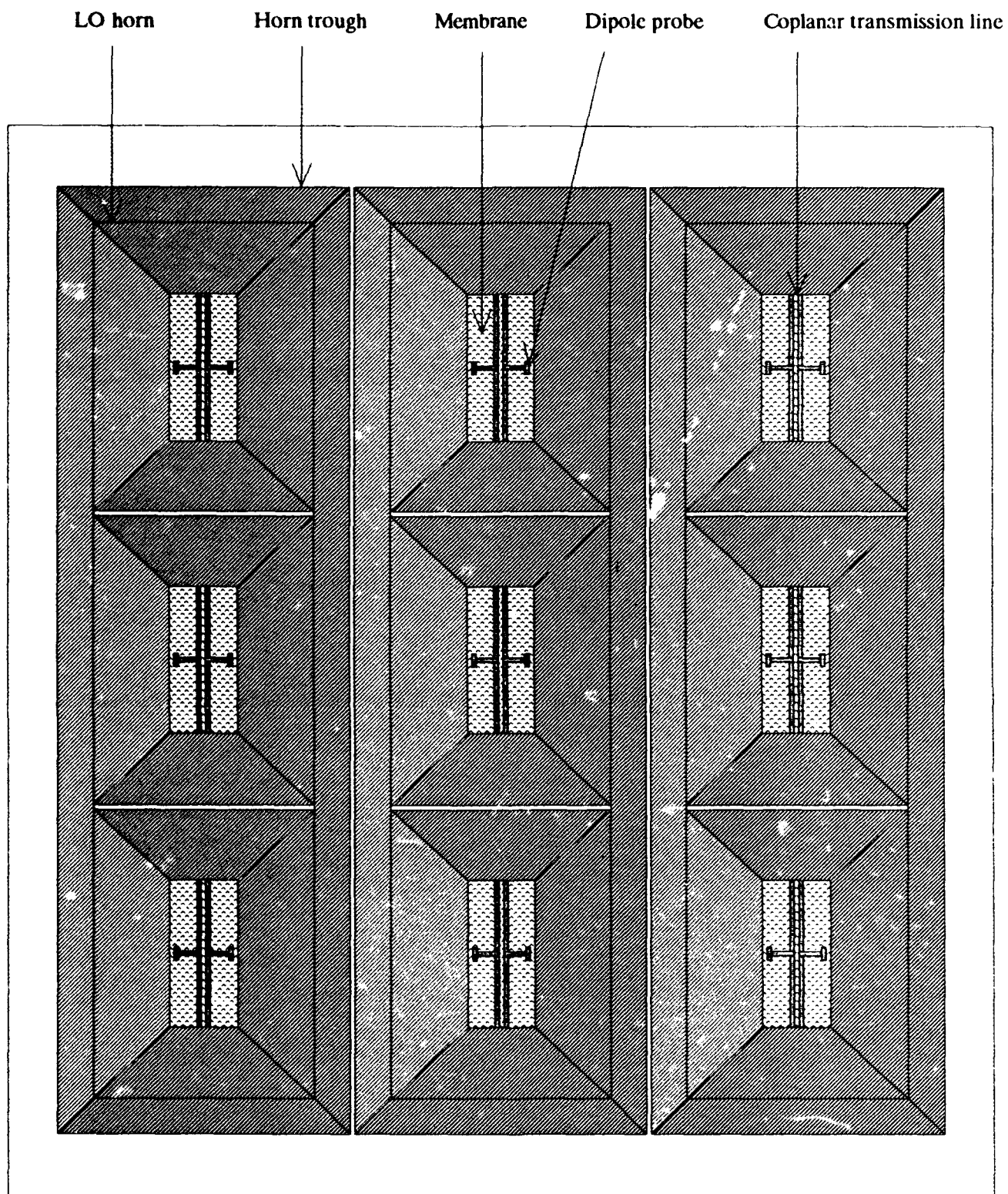
Figure 3. Proposed back-to-back horn array, LO face.

$$P = 1.0 \, \lambda_{RF}$$
$$P_1 = 0.20 \, \lambda_{LO}$$
$$L_1 = 0.26 \, \lambda_{RF}$$
$$L = 0.30 \, \lambda_{RF}$$
$$D = 0.1? \, \lambda_{LO}$$
$$d = 0.08 \, \lambda_{LO}$$
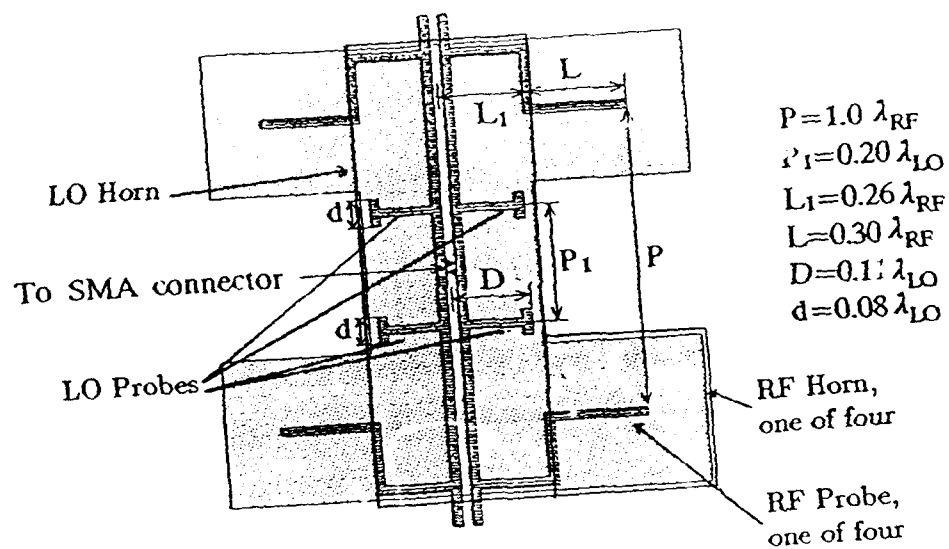
RF and LO Probes on silicon oxynitride membrane.

Start 2.0 GHz
Stop 12.0 GHz
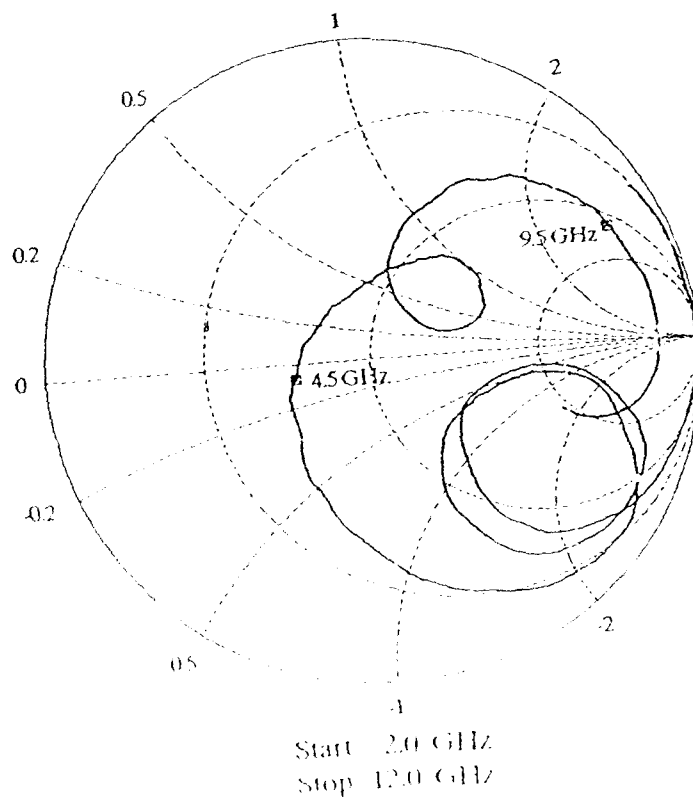
Figure 4. Mixer Configuration and Impedance as seen by the mixer, from microwave model measurements.

horn

membrane
probe

amplifier
gate bias

bonding wires
thermal-electric detector

drain bias

low frequency connection

cavity (etched space)
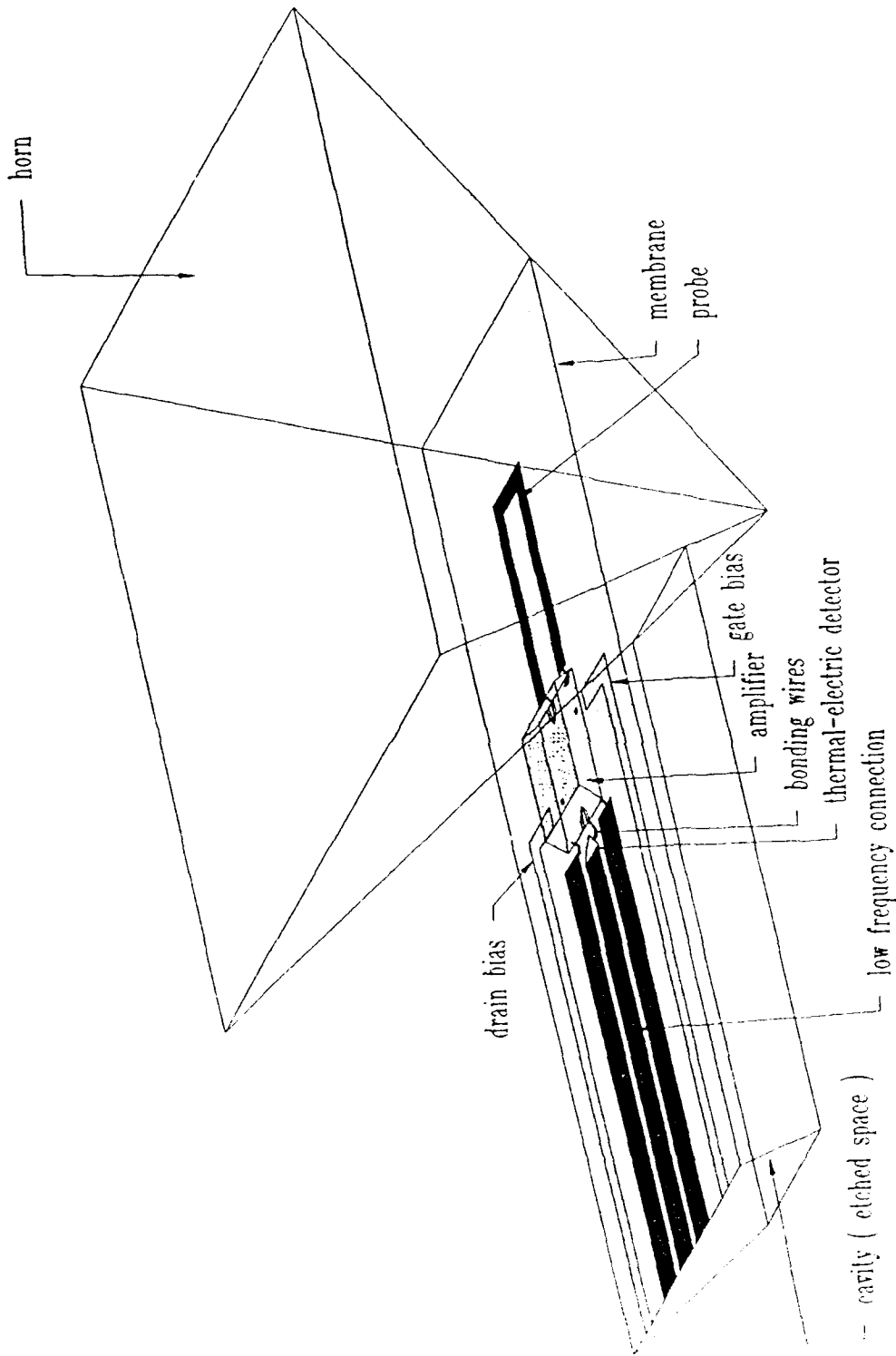
Figure 5. Horn Antenna with HEMT Amplifier. The horn will be etched in silicon wafers; low frequency connections will extend to the edge of the wafer for external attachment.

9

Mag E

3.86e+04

1.42e+02

HFSS
HP 85180A
A.01.00

Mouse Mode
Object   Yes
Grid   Yes
Keyboard No

Maximums
x 7.8660e+00
y 8.0000e+00
z 1.6665e+00

Minimums
x -2.9775e+00
y -1.6665e+00
z -2.0332e+00

Mouse Position
u +0.0000e+00
v +0.0000e+00

mm

Mouse Left
MENU PICK
Mouse Right
MENU PICK

active   zoom 3

Resolving Pointers
Converting Octo
Cleaning Up
Done

110
75
70
105
80
115
100
85
90
95

Start
70

f GHz

Stop
115

Figure 6. Horn and Probe Simulation. Hewlett/Packard High Frequency Structures Simulator screen dump showing field at the horn mouth, and Smith Chart plot of probe impedance. Shown is half the horn, probe and line, vertically split to reduce computation time.

10

Monolithic Millimeter-Wave Two-Dimensional Horn Imaging Arrays

Gabriel M. Rebeiz

Dayalan P. Kasilingam

Yong Guo

Philip A. Stimson

David B. Rutledge

Monolithic Millimeter-Wave Two-Dimensional Horn Imaging Arrays
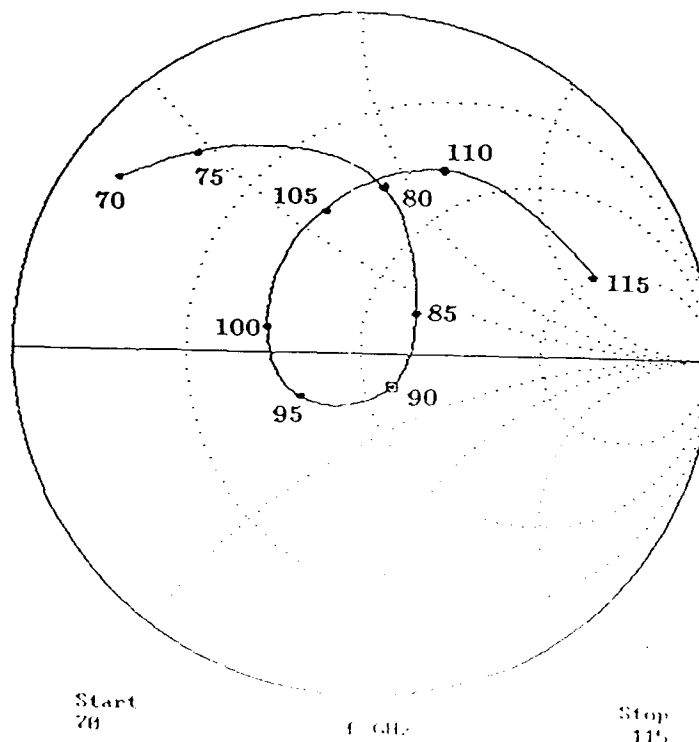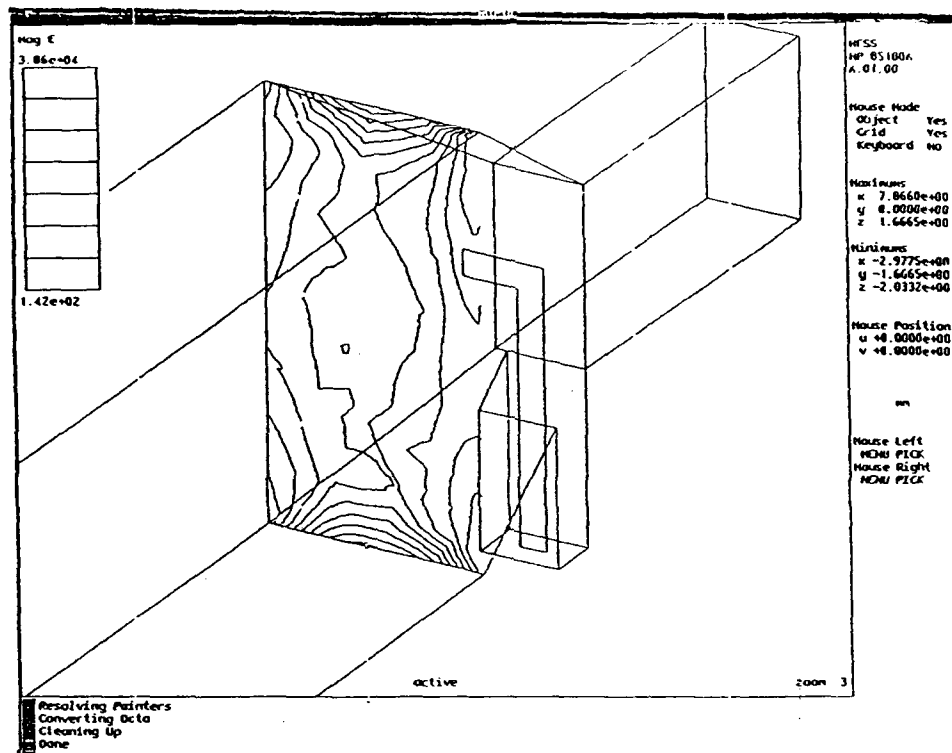
GABRIEL M. REBEIZ, MEMBER, IEEE, DAYALAN P. KASILINGAM, MEMBER, IEEE, YONG GUO,
PHILIP A. STIMSON, AND DAVID B. RUTLEDGE, SENIOR MEMBER, IEEE

Abstract—A monolithic two-dimensional horn imaging array has been fabricated for millimeter wavelengths. In this configuration, a dipole is suspended in an etched pyramidal cavity on a 1-μm silicon-oxynitride membrane. This approach leaves room for low-frequency connections and processing electronics. The theoretical pattern is calculated by approximating the horn structure by a cascade of rectangular-waveguide sections. The boundary conditions are matched at each of the waveguide sections, and at the aperture of the horn. Patterns at 93 and 242 GHz agree well with theory. Horn aperture efficiencies of 44 ± 4%, including mismatch and resistive losses, have been measured. A detailed breakdown of the losses is presented in the paper. The coupling efficiency to various *f*-number imaging systems is investigated, and a coupling efficiency of 24% for an *f* · 0.7 imaging system, including spillover, taper, mismatch and resistive losses, has been measured. Possible application areas include imaging arrays for remote sensing, plasma diagnostics, radiometry and superconducting tunnel-junction receivers for radio astronomy.

I. INTRODUCTION

MILLIMETER-WAVE imaging systems are becoming important in many scientific and military applications [1]-[5]. They provide better resolution than microwave imaging systems and are less affected by atmospheric conditions than infrared systems. The use of a single detector in a mechanically scanned imaging system is a well-established technique for millimeter and submillimeter-wave imaging [1], [2]. However, these scanning systems, whether electronic or mechanical, are inadequate in many applications. The events may be too fast, or the required integration time too long. The way to circumvent this limitation is to image all points simultaneously onto multiple sensors. A millimeter-wave imaging array consists of a large number of antennas with detectors, placed at the focal plane of an imaging system (Fig. 1). The antennas are the feeds for lenses and reflectors in the focusing optics, and the outputs

from all the detectors make up the image. A monolithic focal-plane imaging array is an attractive solution for an imaging array. In these systems, the antennas and detectors are integrated on dielectric substrates such as quartz, silicon and gallium arsenide [6], [7].

Antennas on dielectric substrates suffer from losses to substrate modes [8]. Researchers have attacked this problem in several different ways. Twin-slot [9] and twin-dipole [10] designs reduce the substrate mode power and improve the patterns at the same time. Tapered-slot antennas use the substrate mode on a relatively thin substrate effectively to control the shape of the beam [11]. A lens is often mounted on the back of the substrate to eliminate the substrate modes [6]-[8], at the expense of relatively poor patterns [12] and dielectric absorption losses, which may be severe at submillimeter wavelengths [13]. Recently, however, log-periodic and spiral antennas have shown good patterns with a quartz substrate lens [14], and a two-element Yagi antenna has been successfully demonstrated on a TPX lens [15]. Another way to solve the substrate problem is to integrate the antennas on silicon-oxynitride membranes less than a micron thick. This thickness is so small compared to a wavelength that the antenna effectively radiates in free space. This eliminates the substrate modes and the substrate lens, and allows the use of free-space antenna designs and techniques [16].

Monolithic millimeter-wave imaging arrays have previously been limited to one-dimensional designs, although Yngvesson [11], [17] has made two-dimensional arrays by stacking linear arrays of tapered slot antennas. One problem in two-dimensional arrays is that for efficient reception, the effective area of the antenna must be comparable to the area of the resolution cell, but at the same time there has to be room for electronics and connections. We approach ths problem by fabricating a two-dimensional array of pyramidal horns etched in silicon (Figs. 2, 3). Inside each horn is a probe antenna suspended on a 1-μm thick silicon-oxynitride membrane. The horn collects the energy incident on a resolution cell, and focuses it to the probe antenna on the membrane. All of the probe dipoles, detectors and interconnections are integrated on the same silicon wafer. A major advantage of this approach is that the probe antennas are much smaller than a unit cell; typically the membrane occupies less than 25% of the wafer surface, and the rest of the wafer is available for connections and electronics. The dielectric absorption losses are eliminated and the design can easily be scaled for different wavelengths.
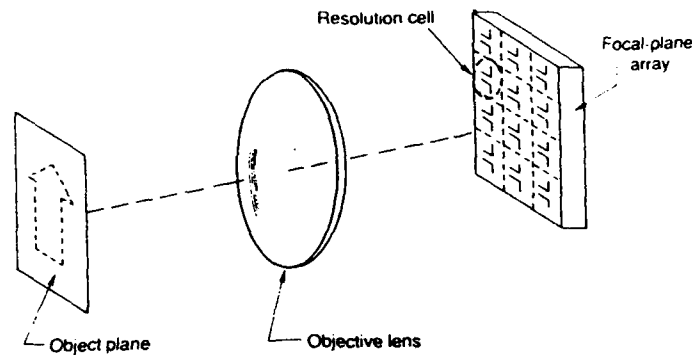
Fig. 1.   Perspective view of a two-dimensional horn imaging array.

Fig. 2.   Millimeter-wave imaging system with a focal-plane imaging array.

Fig. 3.   Side view of a horn array. The 242-GHz array is a two-wafer stack, as shown here. It is also possible to stack more wafers; the 93-GHz array has four wafers. The probe antenna is integrated onto the membrane.

II. FABRICATION

The horn array is a stacked silicon-wafer structure (Fig. 3). The back wafer acts as a reflecting cavity, while the front wafer acts as the mouth of the horn. The openings on the front wafer determine the aperture size of the horn antennas. The thickness of the front wafer determines the position of the probe antennas inside the pyramidal horns. The opening on the back wafer is made equal to the size of the membrane, to result in a pyramidal horn with smooth sidewalls.

The horns are made by anisotropic etching of silicon in an ethylenediamine-pyrocatechol solution [18]. This widely used etchant naturally forms pyramidal holes bounded by $\langle 111 \rangle$ crystal planes in $\langle 100 \rangle$ silicon. The flare angle of the horn is fixed by the orientation of the crystal planes at 70.6°, which is larger than desirable. It may be possible to achieve smaller flare angles with ion-beam milling or reactive-ion etching. It is also necessary to align the mask openings to the $\langle 110 \rangle$ crystal planes, because a misalignment increases the size of the etched pyramidal cavity. To produce the membrane, a silicon oxynitride layer is deposited on the front wafer using plasma enhanced chemical vapor deposition [19], and the silicon etched away to leave the free standing membrane. The

layer must be in tension to yield flat, rigid membranes. Details of this process are available in [20].

After etching, the probe antennas, detectors, and connections are fabricated by standard photolithographic techniques. The horn sidewalls are coated with gold to reduce the resistive losses. The probe antennas are made of silver 1000 Å thick. The detectors are 4 μm-square bismuth microbolometers [21] with a dc resistance of 140 Ω, and a dc responsivity of 10 V/W at a bias of 100 mV. It should also be possible to make superconducting tunnel junctions on the membranes. The wafer stack is made by aligning the wafers in a mask aligner, and gluing them with photoresist spread around the corners. A completed horn is shown in Fig. 4. There is typically a 20 μm step in the pyramidal-cavity sidewalls when any two wafers are joined together. This is due to a

Fig. 6. Forward and backward traveling waves on a waveguide step (left), and a waveguide section (right).

Fig. 4. A scanning electron micrograph of a finished horn element for 242 GHz. The misalignment between the wafers is 20 μm.

Fig. 5. A stepped waveguide approximation of a pyramidal horn. C_0 is the first waveguide and C_m is the membrane waveguide.

slight misalignment with the $\langle 110 \rangle$ crystal planes, and to variations in the wafer thicknesses from batch to batch.

III. THEORY

The theoretical antenna pattern of a single horn-element is calculated assuming an infinite two-dimensional array of horns. It should be noted that we are not calculating the pattern of a phased array, but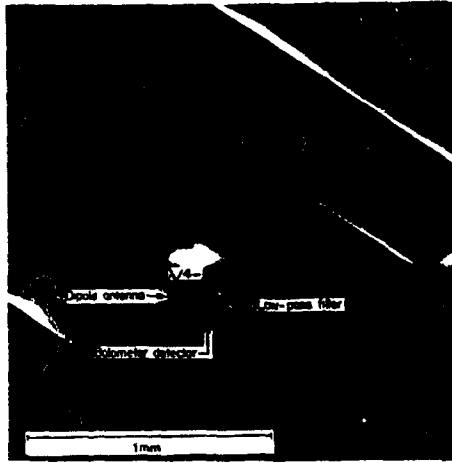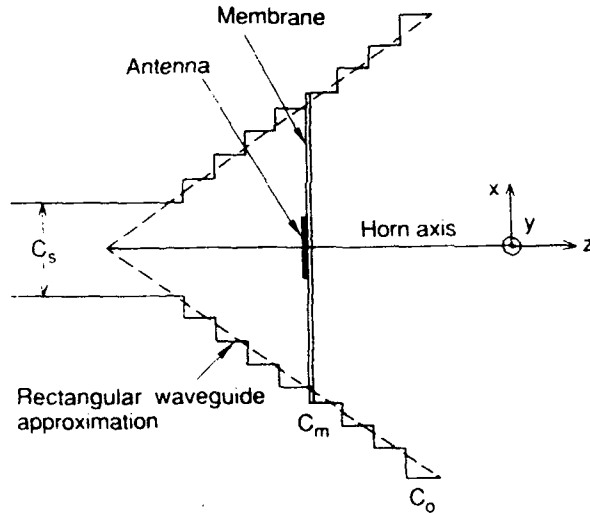 rather the pattern of a single element in a two-dimensional array. This is because we are interested in a focal-plane array of antennas for multibeam imaging applications. Since the horn dimensions are comparable to a free-space wavelength, the horn-array has to be rigorously analyzed using a complete electromagnetic solution. In this analysis, a horn-element is approximated by a structure of multiple rectangular waveguide sections (Fig. 5), and the fields in each waveguide section are given by a linear combination of waveguide modes. This method has been used
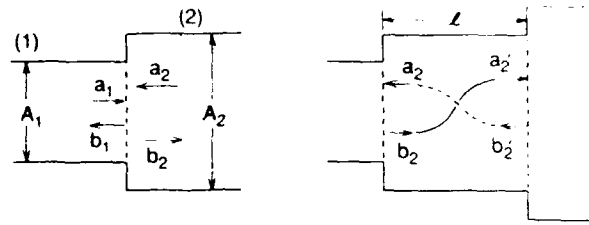
before in the analysis of waveguide transformers [22], and recently applied to the analysis of a corrugated horn [23]. The fields in space are given by two-dimensional Floquet modes [24]. The boundary conditions are matched at each of the waveguide sections, and at the aperture of the horn. The antenna pattern may be calculated by assuming the antenna as either a transmitter or a receiver—the equivalence of these two cases follows from the reciprocity theorem [25]. In our analysis, we assume the horn to be a receiving antenna. The pattern is found by calculating the received fields at the position of an infinitesimal dipole inside the horn, for plane waves incident at different angles. The effect of the membrane on the incident radiation is neglected, since the membrane is very thin compared to a free space wavelength.

A. Pyramidal Horn Characterization

In this section, the scattering matrices of a waveguide-step junction and a linear-waveguide section are derived (Fig. 6). A horn matrix **H** is then calculated, relating the fields in the membrane section C_m to the fields in the opening section C_0. Finally, the Floquet modes in space are matched to the fields in the opening waveguide, and the fields in section C_m are calculated in terms of incident field using the horn matrix **H**.

The transverse fields $(\vec{E}_t, \vec{H}_t)$ in waveguide section (1) Fig. (6) can be represented by a linear combination of transverse electric (TE) and (TM) waveguide modes [26].

$$\vec{E}_t^1 = \sum_{n=0}^{\infty} \sum_{m=0}^{\infty} a_{mn}^{p1} e^{-n\gamma_{mn}^{p1}z} \vec{e}_{mn}^{p1}$$

$$+ \sum_{n=0}^{\infty} \sum_{m=0}^{\infty} b_{mn}^{p1} e^{-n\gamma_{mn}^{p1}z} \vec{e}_{mn}^{p1}$$

$$\hat{z} \times \vec{H}_t^1 = \sum_{n=0}^{\infty} \sum_{m=0}^{\infty} a_{mn}^{p1} Y_{mn}^{p1} e^{-n\gamma_{mn}^{p1}z} \vec{e}_{mn}^{p1}$$

$$- \sum_{n=0}^{\infty} \sum_{m=0}^{\infty} b_{mn}^{p1} Y_{mn}^{p1} e^{+n\gamma_{mn}^{p1}z} \vec{e}_{mn}^{p1} \quad (1)$$

where p denotes either a TE or a TM mode, γ_{mn}^{p1} is the wave propagation constant and is real for a propagating wave and imaginary for an attenuating wave, Y_{mn}^{p1} is the wave admittance for a TE/TM mode, and $\vec{e}_{mn}^{p1}$ is a TE/TM eigenvector normalized such that the power carried by a given wave is proportional to the square of its coefficient $(a_{mn}^{p1}$ or $b_{mn}^{p1})$. The fields in waveguide section (2) follow the same representation. The coefficients a_{mn}^{p1} and b_{mn}^{p1} are unknown, and will be calculated later in terms of the incident field on the horn array. The boundary conditions at the waveguide step junc-

14

tion are the continuity of the transverse electric and magnetic fields over the area A_1, and the vanishing of the transverse electric field on the area $(A_2 - A_1)$. Using the Galerkin mode matching technique [27], we get a set of linear equations

$$\sum_n \sum_m \left(a_{mn}^{p1} + b_{mn}^{p1}\right) V_{mnMN}^{p1p2}$$
$$= a_{MN}^{p2} + b_{MN}^{p2}$$
$$- Y_{mn}^{p1}\left(a_{mn}^{p1} - b_{mn}^{p1}\right)$$
$$= \sum_N \sum_M Y_{MN}^{p2} V_{MNmn}^{p1p2}\left(a_{MN}^{p2} - b_{MN}^{p2}\right) \quad (2)$$

where V_{mnMN}^{p1p2} is the scalar product between a TE/TM eigenvector in waveguide section (1) and a TE/TM eigenvector in waveguide section (2), given by

$$V_{mnMN}^{p1p2} = \int_{A1} \vec{e}_{mn}^{p1} \cdot \vec{e}_{MN}^{p2} \, dA_1. \quad (3)$$

The fields in waveguide section (1) can then be related to the fields in waveguide section (2) through the matrix equation

$$\begin{pmatrix} V & V \\ Y_1 & -Y_1 \end{pmatrix}\begin{pmatrix} a_1 \\ b_1 \end{pmatrix} = \begin{pmatrix} I & I \\ -V^T Y_2 & V^T Y_2 \end{pmatrix}\begin{pmatrix} a_2 \\ b_2 \end{pmatrix} \quad (4)$$

where I is a unit matrix, Y_1 and Y_2 are diagonal admittance matrices of the individual TE/TM modes in sections (1) and (2), respectively. V is a scalar-product matrix of the eigenmodes at the interface, and V^T is the transpose of V. (a_1, b_1) and (a_2, b_2) represent the coefficients of the incident and reflected fields for waveguide sections (1) and (2), respectively.

The fields in a lossless-waveguide section (Fig. 6) are related by a simple phase-delay matrix, given by

$$\begin{pmatrix} a_2 \\ b_2 \end{pmatrix} = \begin{pmatrix} 0 & e^{-j(\gamma_{mn})l} \\ e^{+j(\gamma_{mn})l} & 0 \end{pmatrix}\begin{pmatrix} a'_2 \\ b'_2 \end{pmatrix}. \quad (5)$$

The coefficients of the fields in the membrane section C_m can be related to the coefficients of the fields in the first section C_0 by multiplying the step and delay matrices of a large number of waveguide sections together. The resultant matrix is called the horn matrix $\mathbf{H}$. The smallest waveguide section C_s is chosen to be small enough to have only rapidly decaying evanescent waves. This section is assumed to be an infinite rectangular waveguide with waves traveling only in the negative z-direction. This is important for the numerical solution because large exponential decay constants are avoided. The boundary condition at C_s relates the forward and backward traveling waves in the waveguide sections. This results in only one independent set of variables at C_0 to match to the incident field.

B. Matching to the Floquet Modes

The transverse fields in air $(\vec{E}_t^f, \vec{H}_t^f)$ can be represented by a linear combination of TE and TM Floquet modes [24],

$$\vec{E}_t^f = a_{00}^{pf} e^{+j(\gamma_{00})z} \vec{e}_{00}^{pf} + \sum_{n=-\infty}^{\infty} \sum_{m=-\infty}^{\infty} b_{mn}^{pf} e^{-j(\gamma_{mn})z} \vec{e}_{mn}^{pf}$$

$$\hat{z} \times \vec{H}_t^f = -a_{00}^{pf} Y_{00}^{pf} e^{+j(\gamma_{00})z} \vec{e}_{00}^{pf}$$
$$+ \sum_{n=-\infty}^{\infty} \sum_{m=-\infty}^{\infty} b_{mn}^{pf} Y_{mn}^{pf} e^{-j(\gamma_{mn})z} \vec{e}_{mn}^{pf} \quad (6)$$
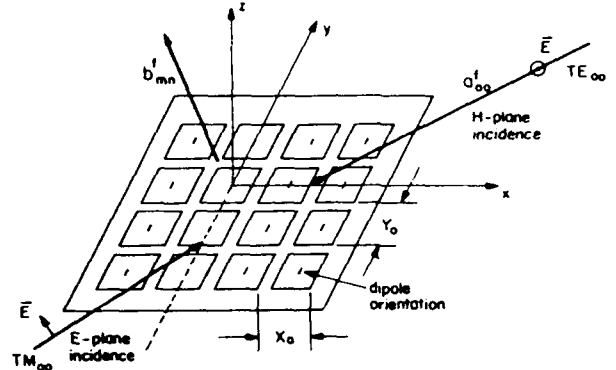

Fig. 7. Incident plane waves for E- and H-plane pattern calculation.

where a_{00}^{pf} and b_{mn}^{pf} are the coefficients of the incident plane wave and the reflected Floquet modes, respectively, and p, γ_{mn}^{pf}, Y_{mn}^{pf} and $\vec{e}_{mn}^{pf}$ are in the same notation as the fields in waveguide section (1). The orthonormalized set of eigenvectors $\vec{e}_{mn}^{pf}$ are derived from the potential function of a plane wave incident on a periodic structure.

The same method is used to match the fields in air to the fields in C_0. The coefficients of the fields in waveguide section C_0 can be related to the coefficients of the fields in air through the matrix equation

$$\begin{pmatrix} F & F \\ Y_0 & -Y_0 \end{pmatrix}\begin{pmatrix} a_0 \\ b_0 \end{pmatrix} = \begin{pmatrix} I & I \\ -F^T Y_f & F^T Y_f \end{pmatrix}\begin{pmatrix} a_f \\ b_f \end{pmatrix} \quad (7)$$

where I is a unit matrix, Y_0 and Y_f are diagonal matrices of the individual waveguide and Floquet modes, and (a_0, b_0) and (a_f, b_f) are the coefficients of the incident and reflected fields for C_0 and air, respectively. F is a matrix of the scalar product between a TE/TM eigenvector in waveguide section C_0 and a TE/TM Floquet eigenvectors in air, given by

$$F_{mnMN}^{p1pf} = \int_{A_0} \vec{e}_{mn}^{p1} \cdot \vec{e}_{MN}^{pf} \, dA_0. \quad (8)$$

The incident field is a plane wave of unit amplitude and its coefficients a_{00}^{pf} are known. The coefficients of the reflected Floquet modes b_{mn}^{pf}, and the coefficients of the waveguide modes a_{mn}^{p0} and b_{mn}^{p0} can be calculated in terms of the coefficients of the incident field. The incident field is a TM$_{00}$ plane wave for the E-plane pattern calculations, and a TE$_{00}$ plane wave for the H-plane pattern (Fig. 7).

The theory developed above is valid for horns with any rectangular cross-section, having an arbitrary separation between the horn apertures. The only condition is that the array is periodic and infinite in extent. The horn was modeled using 50 steps per wavelength, the smallest section C_s being 0.2 λ. In the case of E- and H-plane pattern calculations, only certain waveguide modes are excited because of symmetry. All relevant modes were considered up to $M = N = 7$. The patterns were calculated for square apertures, with the periods of the two-dimensional array, X_0 and Y_0, taken equal to the horn aperture C_0. The separation between the horn openings is neglected, since it is much smaller than C_0.
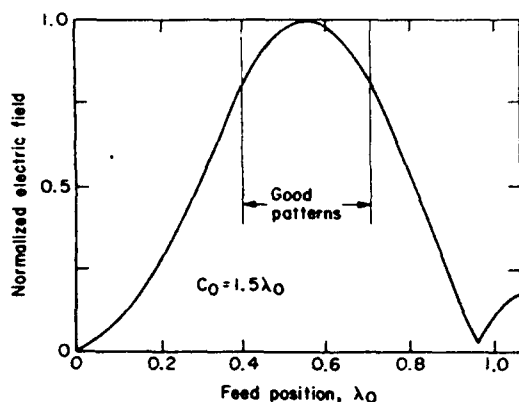
15

Fig. 8 Normalized fields on the horn axis for a plane wave incident normal to the aperture.

Fig. 9. Quarter-wave dipole with a low-pass filter on the membrane.

The horn sidewalls are assumed to be lossless. The following tests were conducted to check the accuracy of the results:

1) Conservation of power—the sum of power in the reflected modes must equal the power in the incident modes. This is true because an infinitesimal dipole does not absorb any power, and the walls are assumed to be lossless.

2) Boundary conditions—the fields at C_0 calculated from the waveguide-modes representation must match the fields calculated from the Floquet-mode representation.

3) Reciprocity theorem—the coupling between any two Floquet modes must remain the same if the incident and reflected modes are interchanged.

IV. DESIGN OF THE HORN STRUCTURE

The horn structure is designed to produce a desirable radiation pattern for an imaging system. The variable parameters are the dimensions of the horn and the position of the dipole inside the horn. Fig. 8 shows the normalized electric field along the horn axis (starting from the apex) for a plane wave incident normal to a 1.5 λ square horn array. At a feed position smaller than 0.35 λ, the membrane cross section is smaller than 0.5 λ, and the fields decrease uniformly because all the waveguide modes are in the cut-off region. There is also a defocusing effect around a feed position of 0.92 λ. The patterns calculated at feed positions of 0.42 λ, 0.56 λ, and 0.71 λ show good horn patterns, indicating a wide horn-bandwidth. Also, the pattern at 0.42 λ was better than the pattern at 0.56 λ. This shows that the point of maximum field intensity is not necessarily the point which gives the best radiation pattern.

Imaging arrays with square horn apertures of 1.0 λ, 1.45 λ and 2.1 λ were fabricated for 242 GHz, and a 1.0 λ array was fabricated for 93 GHz. In all cases, the feed position was 0.39 λ, and the membrane side length was around 0.55 λ. The probe antennas were $\lambda/4$ dipoles with an integrated coplanar-strip isolation filter (Fig. 9). The coplanar strips are designed to have a characteristic impedance of 200 Ω when suspended on the membrane, (calculated from the quasi-static solution to coplanar strips in free space [28]), and an impedance of 4 Ω when sandwiched between two silicon
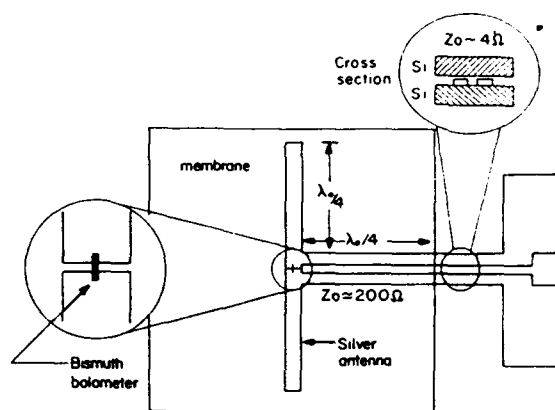
wafers. The quarter-wave section of coplanar strips transforms the 4 Ω impedance into a very large parallel impedance at the dipole apex. The bolometer presents there a much lower impedance, and therefore absorbs all the received power.

V. MEASUREMENTS

Microwave measurements were made on a 3 × 3 scale aluminum model of the 93 GHz array at around 7.3 GHz to determine the impedance of the dipole probe antenna inside the pyramidal cavity. A coaxial line feeds a dipole antenna and a coplanar-strip transmission line which is shorted $\lambda/4$ away from the feed. This design has two purposes. It models the coplanar strips on the membrane effectively, and it provides an effective balun [2] for the coax-dipole feed. The measured impedance, 50 Ω + j95 Ω, is highly inductive. The 93-GHz antenna will have an additional series resistance resulting from loss in the metal. The dipole thickness is only about a third of the skin depth, so that we can safely take the RF series resistance to be the same as the dc series resistance, which is approximately 4 Ω. The estimated 93-GHz antenna impedance is thus $Z_a = 54$ Ω + j95 Ω.

Millimeter-wave measurements were made at 93 GHz and 242 GHz. At 93 GHz, the source was a Varian reflex klystron modulated at 1 kHz with a power output of 80 mW. At 242 GHz, the source was a Millitech waveguide-tripler fed by an 80.7 GHz Gunn diode modulated at 1 kHz. The power output of the tripler was about 1 mW. The detected signal was fed to a lock-in amplifier. Care was taken to reduce scattering from the antenna and source mounts.

Measurements were made in the E- and H-planes and 45° planes of both the co-polarized and cross-polarized components. Full two-dimensional scans were also made of the co-polarized component. Patterns measurements were made on four different elements within the imaging array. Single element patterns are given here; the results for the other elements are very similar. No measurements were made on elements at the edge of the array.

VI. PATTERNS: THEORY VERSUS EXPERIMENT

The measured patterns at 93 and 242 GHz show good agreement with theory (Figs. 10-15). The E-plane pattern of

16
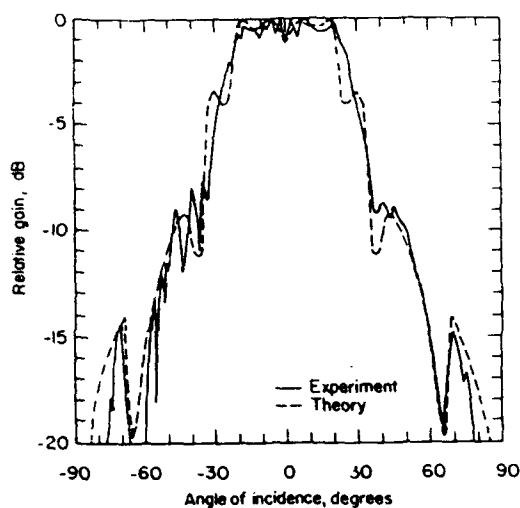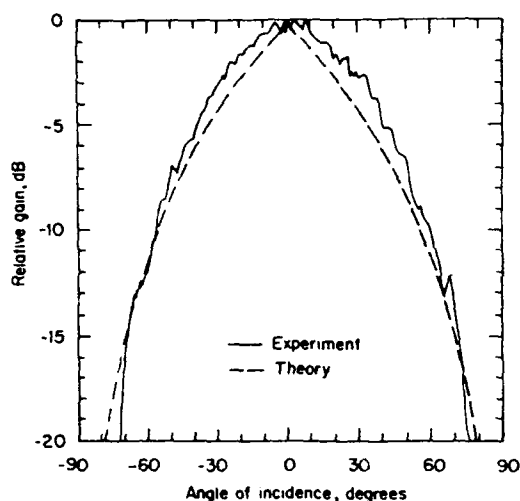
Fig. 10. Typical E-plane (a) and H-plane (b) patterns measured at 93 Ghz on a (7 × 7), 1.0 λ imaging array. Notice the −14 dB sidelobes in the E-plane.

Fig. 11. Typical E-plane (a) and H-plane (b) patterns measured at 242 GHz on a (9 × 9), 1.45 λ imaging array. The zigzags on the measured E-plane pattern are due to scattering from the antenna mount.

the 1.45 λ array measured at 242 GHz does not exhibit any sidelobes. We attribute this to losses in the cavity sidewalls, which were not coated by a gold layer. In contrast, the sidewalls for the 93 GHz array were gold coated, and the E-plane pattern of the 1.0 λ array measured at 93 GHz (Fig. 10) shows slight gain suppression at normal incidence and sidelobes as predicted by the theory. The sidelobes result from the incident energy scattering into successively higher order Floquet modes. A 1.0 λ array was constructed for 242 GHz which did not incorporate gold plating on the horn sidewalls. The measured patterns (not shown) were similar to the 93 GHz 1.0 λ array except for the absence of sidelobes. The discrepancy between theory and experiment in the E-plane pattern of the 2.1 λ arrays (Fig. 12) can also be explained 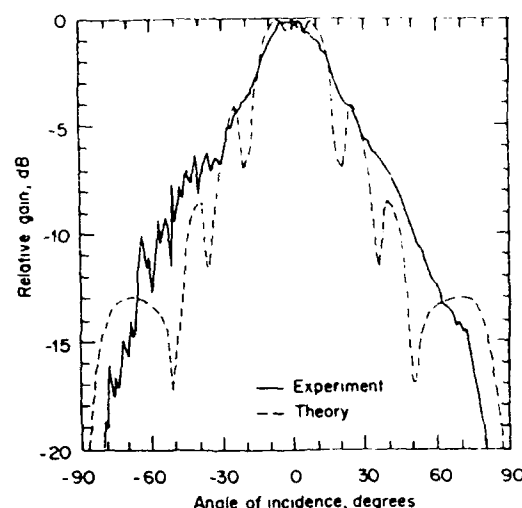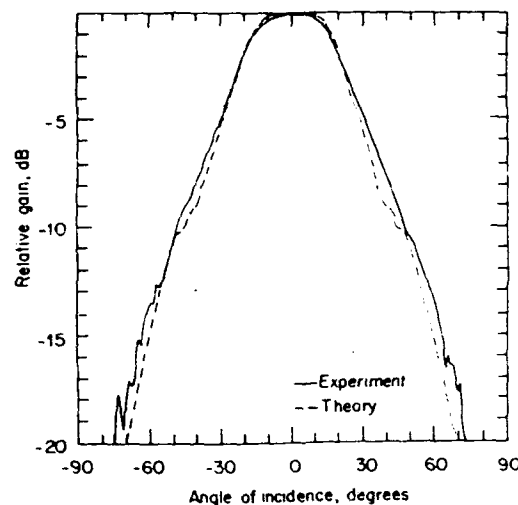by the large resistive sidewall loss. In this case, the cavity was not gold coated, and the silicon wafer was lightly doped.

The horn antennas were linearly polarized parallel to the probe dipole. The cross-polarized component at normal incidence was limited by the noise floor, which ranged from −20 to −30 dB depending on the quality of the bolometers. There was also no measurable cross-polarized component in either the E- or H-planes. This is due to the symmetrical structure of the antenna. The 45° cross-polarized patterns were symmetrical about normal incidence, and showed a peak cross-polarized component at ±60° (Fig. 13).

Tabulated in Table I are the exact dimensions of the imaging arrays, with the corresponding measured 3- and 10-dB beamwidths of the E- and H-plane patterns. The calculated directivities from the co-polarized two-dimensional scans show a decreasing horn-aperture efficiency with increasing aperture size. From a transmitting point of view, a horn with a large aperture is not uniformly illuminated by the dipole and suffers from aperture taper (nonuniform field

17
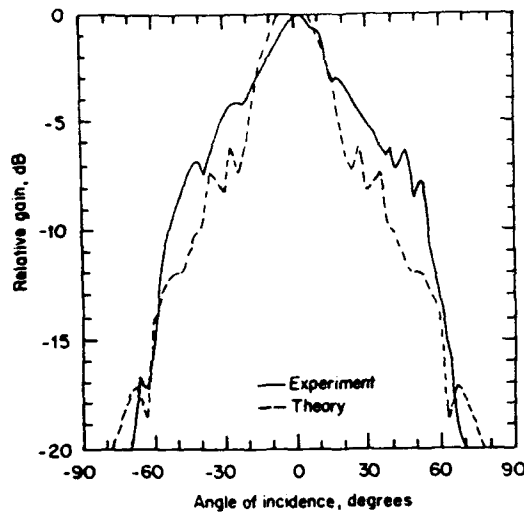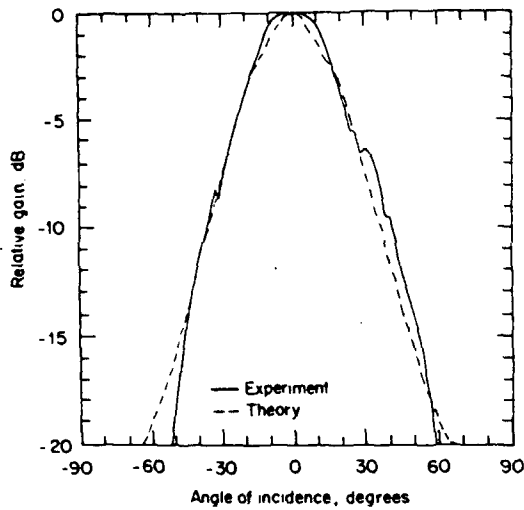
Fig. 12 Typical *E*-plane (a) and *H*-plane (b) patterns measured at 242 GHz on a (7 × 7), 2.1 λ imaging array.

Fig. 13. Typical 45° co-polar and cross-polar plane patterns measured at 242 GHz on a (9 × 9), 1.45 λ imaging array (a), and at 93 GHz on a (7 × 7), 1.0 λ imaging array (b).

distribution) and phase errors. Also, the *H*-plane pattern narrows with increasing aperture size, while the *E*-plane remains the same after 1.45 λ. This is due to the boundary conditions at the horn aperture.

VII. HORN-APERTURE EFFICIENCY AT 93 GHz

The horn-aperture efficiency of a single element in the array is defined as the power received by the bolometer divided by the total power incident on the horn aperture. To measure this, we must calibrate the bolometer, and measure the gain and the power transmitted from the source. Details of the procedure are given in [20]. The measured horn-aperture efficiency is 44 ± 4%, or − 3.6 dB.

It is important to account for the different contributions to the measured loss, because this indicates the potential for improvements. Table II gives the breakdown of the losses. The total calculated losses are 3.4 dB [20]. The largest loss is

the 2.2 dB dipole mismatch loss between the probe dipole and the bolometer. It is given by the formula $4R_a R_b / |Z_a + R_b|^2$, where R_a is the antenna radiation resistance (50 Ω), R_b is the bolometer resistance (138 Ω), and Z_a is the antenna impedance (54 + j95 Ω). The next biggest loss is resistive loss in the horn sidewalls, which is equal to 0.7 dB. In this case, the 93 GHz horn array was assembled from four different stacked wafers, and the membrane wafer was not gold coated. It should be possible to reduce the mismatch and wall losses, if all the horn sidewalls are gold coated, and the antenna is matched. The aperture efficiency of a 1.0 λ square horn should then be around 88%.

VIII. SYSTEM COUPLING EFFICIENCY MEASUREMENTS

The coupling efficiency to an imaging system is defined as the power received by a single element placed at the focal point of an imaging system, divided by the total power

18
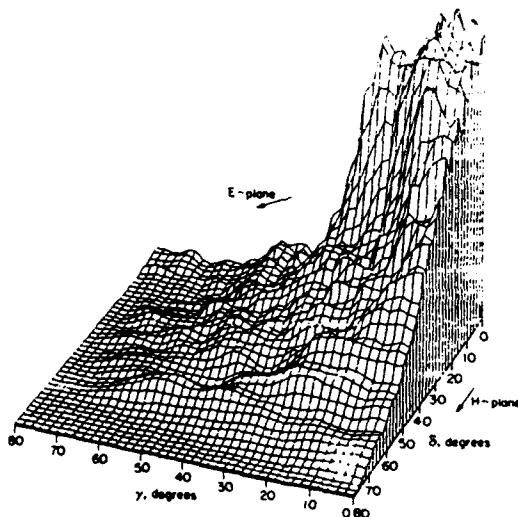
Fig. 14. Measured two-dimensional scans of a (7 × 7) array at 93 GHz. Vertical scale is linear in power.

Fig. 15. Measured two-dimensional scans of a (9 × 9) array at 242 Ghz. Vertical scale is linear in power.

TABLE II

CALCULATED AND·MEASURED HORN APERTURE-EFFICIENCY LOSSES

Intrinsic Pattern Loss	-0.2 dB
Mismatch Loss	-2.2 dB
Horn Sidewall Loss	-0.7 dB
Cross-Polarization Loss	-0.2 dB
Horn-to-Horn Coupling Loss	-0.1 dB
Total Calculated Loss	-3.4 dB
Total Measured Loss	-3.6 dB
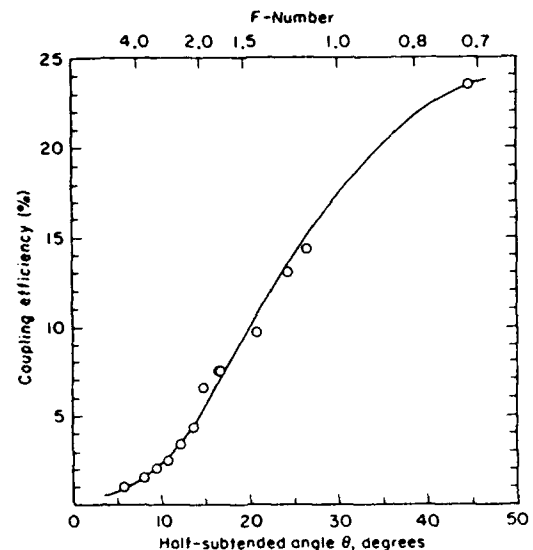
Fig. 16. Coupling efficiency of a horn element in a 1.0 λ imaging array. Measured points, indicated by circles, include the mismatch and resistive losses in the horn element, and the taper and spillover losses of the lens.
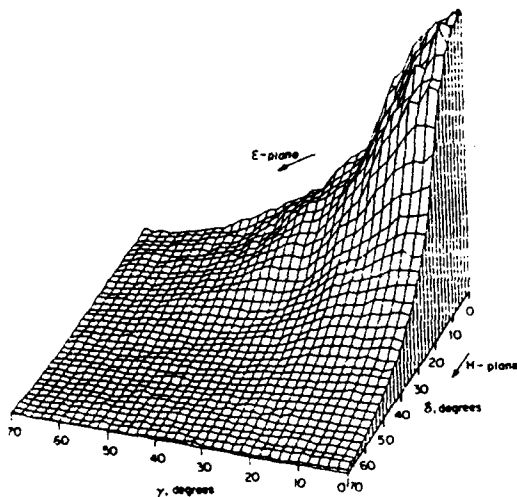
incident on the primary lens, when the lens is illuminated by a plane wave. The coupling efficiency of the 1.0 λ imaging array was measured at 93 GHz for systems of different *f*-number (Fig. 16). These were produced by placing aperture-stops over the lens. We found that 24% of the incident power is absorbed by a single detector for an *f*-number of 0.7, and 14% for an *f*-number of 1.1. If matching and sidewall losses were eliminated, the efficiency would be 54%. This agrees with the theoretical coupling-efficiency of 60% [30].

The distribution of power in the focal plane, for an incident plane-wave normal to the lens, was measured for two separate lenses with *f*-numbers of 1.1 and 0.7, respectively (Fig. 17). The sum of the total power on the focal plane yields a total coupling efficiency of 25% for both lenses. The lens Airy pattern [31] has a first dark-ring radius of 0.61 λ and 1.22 λ for an *f* 0.7 and *f* 1.1 lens, respectively. The center element receives 96% of the total power incident on the focal plane for an *f* 0.7 lens, and 56% for an *f* 1.1 lens. There is then a strong optical coupling between the elements for an *f* 1.1 lens, i.e., for a diffraction limited imaging array. Hence, a significant fraction of the power appropriated to the central element is distributed among adjacent elements, and this central element also receives power appropriated to its neighbors. This optical coupling

TABLE I

MEASURED 3-dB AND 10-dB BEAMWIDTHS OF SEVERAL MILLIMETER-WAVE IMAGING ARRAYS.

Array	1.0 λ	1.45 λ	2.1 λ
f GHz	93	242	242
C_0/λ	1.01	1.42	2.09
Sep /λ	0.02	0.03	0.02
S_{mbr}	25%	13.5%	7.5%
E(3-dB)	54°	35°	35°
E(10-dB)	100°	95°	97°
H(3-dB)	62°	46°	32°
H(10-dB)	110°	90°	70°
D.	11.9	17.3	21
ϵ_{ap}	95%	67%	38%

"Sep " is the separation between two openings C_0, and S_{mbr} is the percentage of the space on the wafer occupied by the membranes and the antennas

Fig. 17   Distribution of power in the focal plane as a percentage of the total power incident on the lens, for $f \cdot 0.7$ lens (a) and $f \cdot 1.1$ lens (b).

will blur the image, although in principle, the information is recoverable by coherent processing. On the other hand, the optical coupling in a $f \cdot 0.7$ system is negligible, and the coupling efficiency to the central element is much larger. The penalty paid is an undersampling of the image.

IX. CONCLUSION

A new monolithic millimeter-wave two-dimensional horn imaging array has been presented. This novel configuration allows ample space for low-frequency interconnections, while still maintaining efficient diffraction-limited imaging. The array is analyzed rigorously by approximating the horn antenna by a structure of multiple rectangular waveguide sections. Pattern measurements at 93 and 242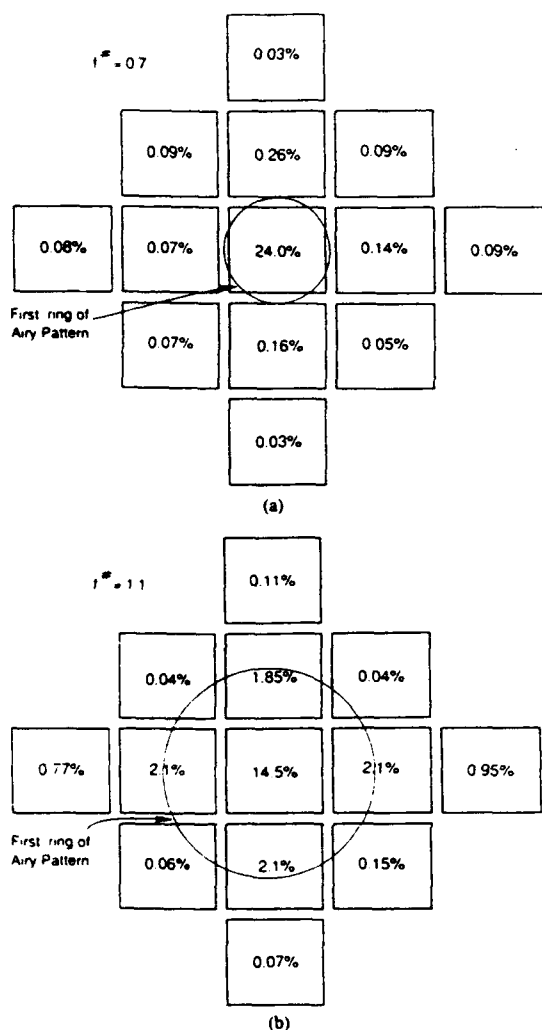 GHz agree well with the theory, and display a centralized peak in the E- and H-plane patterns. The results show that horn antennas with an opening between 1.0 λ and 1.5 λ have high aperture efficiencies and would couple to appropriate imaging systems well. A horn aperture efficiency of 44% ± 4% was measured

at 93 GHz on a 1.0 λ imaging array. Microwave modeling at 7.3 GHz indicates that the major loss component is the mismatch loss between the probe dipole and the detector. The other main contribution arises from the horn sidewalls. It should be possible to reduce the mismatch and wall losses, and thus result in a 1.0 λ imaging array with an aperture efficiency around 88%. A system coupling efficiency of 24% has been measured at 93 GHz for a $f/0.7$ imaging system including spillover, taper, mismatch and resistive losses. The distribution of power in the focal plane indicate that the imaging array is well suited for diffraction-limited imaging. Finally, the horn-array could be used as a monolithic phased array, with the power combiners and phase shifters occupying the available space near the antennas.

REFERENCES

[1]   W. J. Wilson, R. J. Howard, A. C. Ibbott, G. S. Parks and W. B. Ricketts, "Millimeter-wave imaging sensor," IEEE Trans. Microwave Theory Tech., vol. MTT-34, pp. 1026-1035, 1986.

[2]   J. P. Hollinger, "A versatile millimeter-wave imaging system," IEEE Trans. Microwave Theory Tech., vol. MTT-24, pp. 786-793, 1976.

[3]   E. K. Reedy, G. W. Ewell, "Millimeter Radar," in Infrared and Millimeter Waves, vol. 4, K. J. Button, Ed. New York: Academic, 1983, pp. 23-94.

[4]   P. E. Young, D. P. Neikirk, P. P. Tong, D. B. Rutledge, and N. C. Luhmann, "Multichannel far-infrared imaging for fusion plasmas." Rev. Sci. Instrum., vol. 56, pp. 81-89, 1985.

[5]   T. G. Phillips and D. B. Rutledge, "Superconducting tunnel detectors in radio astronomy," Sci. American, vol. 254, pp. 96-102, 1986.

[6]   C. Zah, D. P. Kasilingam, J. S. Smith, D. B. Rutledge, T. Wang, and S. E. Schwarz, "Millimeter-wave monolithic Schottky diode imaging arrays," Int. J. Infrared Millimeter Waves, vol. 6, pp. 981-997, 1985.

[7]   D. B. Rutledge and M. S. Muha, "Imaging antenna arrays," IEEE Trans. Antennas Propagat., vol. AP-30, pp. 535-540, July 1982.

[8]   D. B. Rutledge, D. P. Neikirk, and D. P. Kasilingam, "Integrated-circuit antennas," in Infrared and Millimeter Waves, vol. 10, K. J. Button, Ed. New York: Academic, 1983, pp. 1-90. (Note: The argument k of the elliptic functions of equation (23) should be $\tan^2(45° - \theta/4)$, rather than $\tan(45° - \theta/4)$, where θ refers to the full bow angle.)

[9]   R. L. Rogers, D. P. Neikirk, and H. Ling, "Planar matching of antennas on electrically thick dielectric substrates," in Proc. 12th Int. Conf. Infrared Millimeter Waves, Lake Buena Vista, Dec. 1987, pp. 288-289.

[10] W. Chu and H. R. Fetterman, "Printed circuit antennas and FET detectors for millimeter-wave imaging," in Proc. 12th Int. Conf. Infrared Millimeter Waves, Lake Buena Vista, Dec. 1987, pp. 222-223.

[11] K. S. Yngvesson, D. H. Schaubert, T. L. Korzeniowski, E. L. Kollberg, T. Thungren and J. F. Johansson, "Endfire tapered slot antennas on dielectric substrates," IEEE Trans. Antennas Propagat., vol. AP-33, pp. 1392-1400, Dec. 1985.

[12] R. C. Compton, R. C. McPhedran, Z. Popović, G. M. Rebeiz, P. P. Tong and D. B. Rutledge, "Bow-tie antennas on a dielectric half-space. Theory and experiment," IEEE Trans. Antennas Propagat., vol. AP-35, pp. 622-631, June 1987.

[13] M. N. Afsar, "Dielectric measurements of millimeter-wave materials," IEEE Trans. Microwave Theory Tech., vol. MTT-32, pp. 1598-1609, 1984.

[14] K. Lee and M. Frerking, "Planar antennas on thick dielectric sub-

strates," in *Proc. 12th Int. Conf. Infrared Millimeter Waves*, Lake Buena Vista, Dec. 1987, pp. 216-217.

[15] K. Mizuno, K. Uehara, H. Nishimura, T. Yonekura, and T. Suzuki, "Yagi-Uda array for millimeter-wave imaging," *Electron. Lett.*, submitted.

[16] G. M. Rebeiz, W. G. Regehr, D. B. Rutledge, R. L. Savage, and N. C. Luhmann Jr., "Submillimeter-wave antennas on thin membranes," *Int. J. Infrared Millimeter Waves*, vol. 8, pp. 1249-1256, Oct. 1987.

[17] K. S. Yngvesson, J. F. Johansson, and E. L. Kollberg, "A new integrated slot element feed array for multibeam systems," *IEEE Trans. Antennas Propagat.*, vol. AP-34, pp. 1372-1376, Nov. 1986.

[18] K. E. Peterson, "Silicon as a mechanical material," *Proc. IEEE*, vol. 70, pp. 420-457, May 1982.

[19] D. W. Hess, "Plasma-enhanced CVD: Oxides, nitrides, transition metals, and transition silicides," *J. Vac. Sci. Technol.*, vol. 2, pp. 244-252, Apr.-June 1984.

[20] G. M. Rebeiz, "Monolithic millimeter-wave two-dimensional horn imaging arrays," Ph.D. dissertation, California Inst. Technol., Pasadena, CA, 1988.

[21] D. P. Neikirk, W. W. Lam, and D. B. Rutledge, "Far-infrared microbolometer detectors," *Int. J. Infrared and Millimeter Waves*, vol. 5, pp. 245-278, 1984.

[22] H. Patzelt and F. Arndt, "Double-plane steps in rectangular waveguides and their applications for transformers, irises and filters," *IEEE Trans. Microwave Theory Tech.*, vol. MTT-30, pp. 771-776, May 1982.

[23] J. A. Encinar and J. M. Rebollar, "A hybrid technique for analyzing corrugated and noncorrugated rectangular horns," *IEEE Trans. Antennas Propagat.*, vol. AP-34, pp. 961-968, Sept. 1986.

[24] N. Amitay, V. Galindo, and C. P. Wu, *Theory and Analysis of Phased Array Antennas*. New York: Wiley, 1972, pp. 37-44.

[25] R. S. Elliott, *Antenna Theory and Design*. Englewood Cliffs, NJ: Prentice-Hall, 1981, pp. 41-46.

[26] R. F. Harrington, *Time-Harmonic Electromagnetic Fields*. New York: McGraw-Hill, 1961.

[27] ——, *Fields Computation by the Methods of Moments*. New York: MacMillan, 1968.

[28] K. C. Gupta, R. Garg, and I. J. Bahl, *Microstrip Lines and Slotlines*. Dedham, MA: Artech House, 1979, pp. 195-213.

[29] O. M. Woodward, Jr., "Balance measurements on Balun transformers," *Electron.*, vol. 26, pp. 188-191, Sept. 1953.

[30] D. P. Kasilingam, "Topics in millimeter-wave imaging arrays," Ph.D. dissertation, California Inst. Technol., Pasadena, CA, June 1987.

[31] E. Hecht and A. Zajec, *Optics*. Reading, MA: Addison-Wesley, 1979, ch. 10.

Dayalan P. Kasilingam (S'86-M'86) was born in Colombo, Sri Lanka, on October 24, 1959. He received the B.A. degree in electrical sciences from the University of Cambridge, England, in 1981, and the M.S. and Ph.D. degrees in electrical engineering from the California Institute of Technology, Pasadena, in 1985 and 1987, respectively.

While at Caltech he was a Teaching Assistant in electromagnetic engineering. He joined Ocean Research and Engineering, Pasadena, CA, in December 1986 and has been working on microwave remote sensing of the ocean. His research interests are synthetic aperture radar, radar backscatter from the ocean, polarimetry, adaptive signal processing and stereophotography.

Yong Guo was born in Xian, China, on September 1, 1960. He received the B.S. degree in semiconductor physics from Xian Jiaotong University, Xian, China, in 1982, and the M.S. degree from the California Institute of Technology, Pasadena, in 1987.

He worked at Nanjing Electronic Devices Research Institute, Nanjing, China until 1986. He is currently doing graduate work leading to his Ph.D. degree in electrical engineering at the California Institute of Technology. His interests include millimeter-wave technology and semiconductor devices.

Philip A. Stimson was born in Armidale, Australia, in 1959. He received the B.Sc. (Hons) degree from the University of New England, Australia, in 1981 and the Ph.D. degree in physics from the University of Sydney, Australia, in 1987.

He has worked at the Australian National Measurement Laboratory (1987), the California Institute of Technology (1988-1989) and is currently at the Jet Propulsion Laboratory, Pasadena, CA. His interests include millimeter-wave technology, lasers and microfabrication of components for these devices.

Gabriel M. Rebeiz (S'86-M'88) was born in Beirut, Lebanon, in 1964. He received the B.E. degree in electrical engineering with distinction from the American University of Beirut in 1982, and the Ph.D. degree in electrical engineering from the California Institute of Technology, Pasadena, in 1988.

He joined the University of Michigan, Ann Arbor, in September 1988 as an Assistant Professor in Electrical Engineering and Computer Science. He has worked on the design, fabrication and measurement of microwave and millimeter-wave antennas, circuits and devices. He developed a wideband log-periodic antenna (100-1500 GHz) on thin silicon-oxynitride membranes, invented a new monolithic two-dimensional horn array (94 GHz, 240 GHz) for efficient diffraction-limited millimeter-wave imaging, and designed and tested large-area bolometers for absolute power calibration at millimeter and submillimeter wavelengths. He is currently establishing the Terahertz Integrated Circuits and Systems (TICS) group at the University of Michigan with research interests in millimeter-wave and submillimeter-wave integrated antennas, radiometers, and phased-arrays.

David B. Rutledge (M'75-S'77-M'77-S'78-M'80-SM'89) was born in Savannah, GA, on January 12, 1952. He received the B.A. degree in mathematics from Williams College, Williamstown, MA, in 1973, the M.A. degree in electrical sciences from Cambridge University, Cambridge, England, in 1975, and the Ph.D. degree in electrical engineering from the University of California, Berkeley, in 1980.

In 1980 he joined the faculty at the California Institute of Technology, Pasadena, where he is now Professor of Electrical Engineering. His research is in developing millimeter and submillimeter-wave monolithic integrated circuits and applications, and in software for computer-aided design and measurement. He is co-author with Professor Richard Compton of Cornell University of the software CAD program, *Puff*, which has over 6000 users worldwide.

21

Thin-Film Power-Density Meter for Millimeter Wavelengths

Karen A. Lee, Yong Guo, Philip A. Stimson,
Kent A. Potter, Jung-Chih Chiao, and
David B. Rutledge

Abstract—A quasi-optical power-density meter for millimeter and submillimeter wavelengths has been developed. The devi· is a 2-cm square thin-film bismuth bolometer deposited on a mylar membrane. The resistance respositivity is $150\,\Omega/W$ and the time constant is one minute. The meter is calibrated at DC. The bolometer is much thinner than a wavelength and thus can be modeled as a lumped resistance in a transmission-line equivalent circuit. The absorption coefficient is 0.5 for $189\ \Omega/$square film. As an application, the power-density meter has been used to measure absolute power densities for millimeter-wave antenna efficiency measurements. We have measured absolute power densities of $0.5\ mW/cm^2$ to an estimated accuracy of 5%.

I. INTRODUCTION

In measuring millimeter-wave antenna efficiencies, knowing the absolute power density at the receiving antenna is essential. Relative power-density measurements at millimeter and submillimeter wavelengths are readily performed using commercial detectors. These
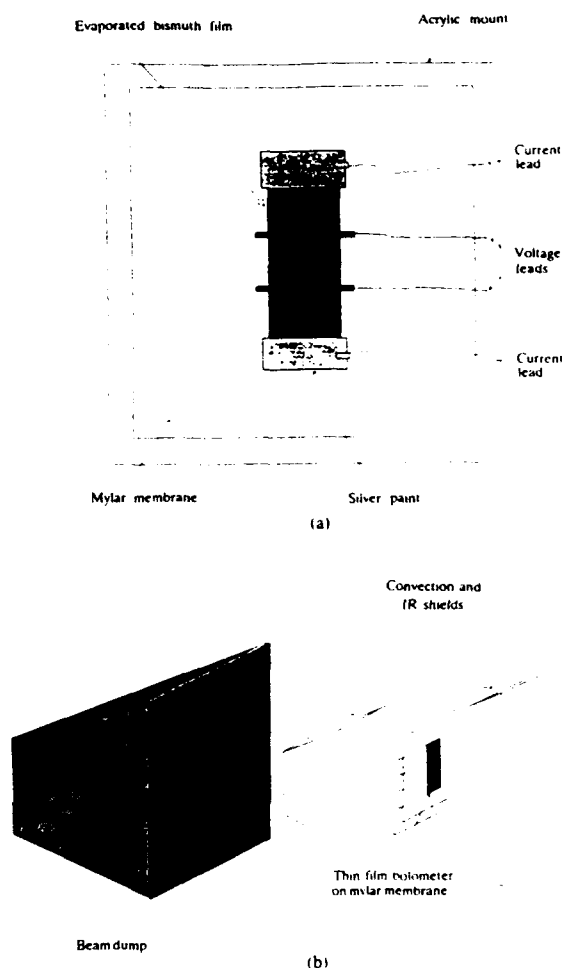
Fig. 1.   (a) Thin-film bolometer on a membrane. (b) Power-density meter with bolometer embedded in styrofoam.

consist of two principal types: quasi-optical power meters in which the radiation is incident on an absorbing element in free space [1], and waveguide power meters in which the radiation is coupled by a horn to fundamental-mode waveguide and absorbed by an element in the guide. However, absolute power-density measurements are more difficult. With the quasi-optical power meters the uncertainty comes about from not knowing accurately the absorption coefficient of the detector element. This problem also exists in the waveguide power meters. Other problems with waveguide power-meter measurements are the repeatability of connections, calibration of directional couplers, and the uncertainty in standard-gains horns.

Recently, there has been interest in millimeter-wave power-density meters whose absorption coefficient is accurately known and whose response can be calibrated at low frequencies. In one approach, developed by Derek Martin, radiation is absorbed in a metallic thin film suspended in a gas cell, and a microphone detects the resulting pressure change [2]. An accuracy of 10% is quoted. Another approach consists of a thin-film bolometer on a silicon-oxynitride membrane whose responsivity is calibrated with an amplitude-modulated ac current. The resistance change resulting from the incident chopped millimeter-wave signal is measured with a lock-in amplifier [3].

Our meter is a simple design consisting of an evaporated bismuth film on a mylar membrane (Fig. 1(a)). There are no vacuum windows and the device is easy to fabricate. Calibration is per-

formed with dc measurements only. This means that no chopping factors or frequency roll-off corrections are required. The device is polarization independent and the reception patterns are smooth, with no spikes at normal incidence. A primary application for this device is absolute power calibration for antenna efficiency measurements.

II. DESCRIPTION AND FABRICATION

A bolometer is a thermal detector whose resistance change is proportional to its thermal impedance. The resistance responsivity in Ω/W is given by

$$\mathcal{R}_\Omega = a\alpha R_e R_t \tag{1}$$

where a is the millimeter-wave absorptance, α is the temperature coefficient of the bolometer material, R_e is the electrical resistance, and R_t is the thermal resistance. We have constructed our bolometer on a 5-μm mylar membrane in order to increase the thermal resistance of the device. The bolometer is surrounded by 5-cm styrofoam blocks to reduce convection heat loss to the air and to block infrared radiation. The bolometer has a time constant of 1 min, which appears to be determined by thermal diffusion through the styrofoam. The attenuation at 93 GHz in the styrofoam was measured to be less than 0.01 dB/cm so that its effect on our measurements is negligible. By placing the structure in an absorbing beam dump, reflections and other unwanted signals are minimized (Fig. 1(b)).

The bismuth film was evaporated through a metal mask onto the mylar until the dc sheet resistance was 189 Ω. The thickness was about 500 Å. This sheet resistance gives the maximum absorptance by a thin film, 0.5, and is insensitive to small changes in the resistance and the angle of incidence. In addition, the absorptance is independent of polarization and frequency. We have chosen bismuth as the bolometer material because of its high temperature coefficient, measured to be 0.0026 K^{-1}. The geometry of the device allows for a four-point measurement which eliminates the effect of resistance in the contacts because the biasing leads are separate from the voltage sensing leads. The bolometer is square and much thinner than the skin depth in bismuth at millimeter and submillimeter wavelengths (5 μm at 93 GHz), so the RF sheet resistance is the same as the dc resistance.

III. CALIBRATION AND MEASUREMENT

The power density is determined from the resistance change due to millimeter-wave power. Fig. 2 shows a typical measurement sequence. All voltage and current measurements are made with a Hewlett-Packard 6½-digit multimeter. We need to wait at least 5 min before making a resistance measurement to allow for the long time constant of the bolometer. We multiply the resistance change by the responsivity to get the power density. The meter is calibrated by a similar measurement sequence with a known amount of dc power, and then making a correction for the absorptivity to get the millimeter-wave responsivity. There is a resistance drift, which is typically 0.1 Ω/hour. We correct for the drift by taking the average of two readings at different times.

IV. SYSTEMATIC CHECKS

To obtain accurate absolute power measurements from the meter, edge effects and the effects of the biasing contacts and the voltage sensing leads should be negligible. To check for these effects, several bolometers of different sizes were constructed. The measurements from the different bolometers agreed to within ±2%. The results are shown in Table I. The bolometer response was also measured as a function of incident angle (Fig. 3). We can use the transmission-line model to calculate the received power as a function of the angle of incidence $P(\theta)$. When the sheet resistance is half the free-space impedance, the pattern is independent of the
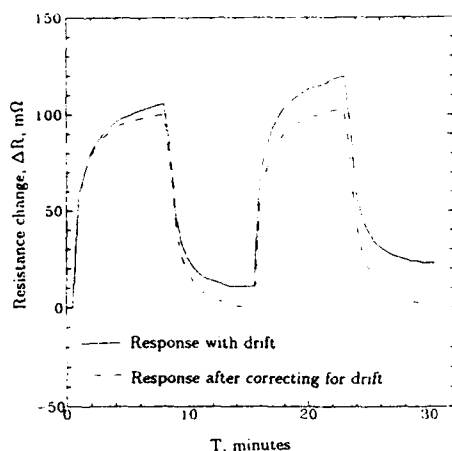
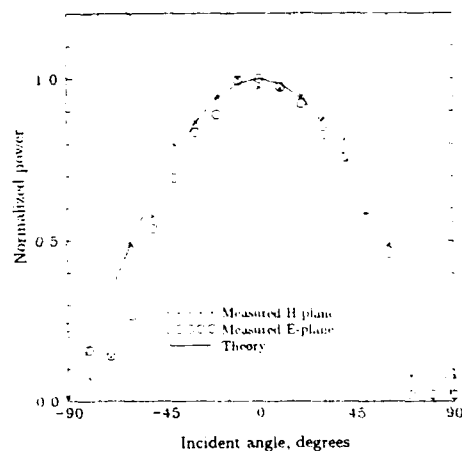Fig. 2. Response to blocked and incident millimeter-wave power.

Fig. 5. Aperture efficiency measurement of horn antenna arrays at 93 GHz.

TABLE 1
POWER DENSITIES MEASURED WITH DIFFERENT BOLOMETERS AT 93 GHz;
SAMPLE STANDARD DEVIATION IS 1.2%

Width (cm)	Length (cm)	Power density (μW/cm^2)
2.0	2.0	575
2.0	1.5	565
2.0	1.0	564
1.5	2.0	582
1.0	2.0	569

polarization and given by

$$P(\theta) = \frac{2\cos^2\theta}{\left(1 + \cos\theta\right)^2} \qquad (2)$$

where θ is the incident angle. The measurements agreed well with the theory. There are no spikes near normal incidence [4].

At higher frequencies, the finite thickness of the mylar membrane will affect the absorptance of the film, and this must be corrected. The calculated correction factors are shown in Fig. 4. For mylar, the refractive index is taken from [5]. The correction is 5% at 2 THz. Alternatively, the thickness of the membrane could be reduced to avoid using the correction [3]. In addition, the absorptance of the styrofoam may affect the measurement and this would need to be checked.

Fig. 3. Measured response to vertically polarized radiation in the E-plane and H-plane as a function of incident angle at 93 GHz. The received power at angles greater than 60° is reduced by blockage from the mount.

V. APPLICATION: ANTENNA EFFICIENCY MEASUREMENT AT 93 GHz

The power-density meter was developed to make accurate aperture efficiency measurements on horns at 93 GHz. These antennas are fabricated on a silicon wafer with integrated microbolometers [6]. The aperture efficiency is the ratio of the power received by the microbolometer in the horn to the power incident on the aperture. The horns are placed in the far field of a source (Fig. 5) and the change in resistance of the microbolometer is measured. The power-density meter is placed at the same location and its change in resistance is measured. The aperture efficiency η of a horn is given by a simple formula

$$\eta = \frac{A_m \mathcal{R}_m \Delta R_a}{A_a \mathcal{R}_a \Delta R_m} \qquad (3)$$

where A is the area, $\mathcal{R}$ is the resistance responsivity, ΔR is the resistance change, and the subscripts m and a denote the power-density meter and the antenna respectively.

Alternatively, the power-density measurement can be related to the reading on the waveguide power meter in Fig. 5. This makes it unnecessary to calibrate the directional coupler, attenuator, and horn individually.

Fig. 4. Calculated absorptance of the power-density meter at higher frequencies

VI. Conclusion

By using a metal film bolometer, we made accurate absolute power measurements at 93 GHz. The calibration procedure is simple and accurate to within 5%, and the actual measurement involves knowing only a few fundamental parameters. This device is useful for measuring millimeter-wave antenna aperture efficiencies.

References

[1]   F. B. Foote, D. T. Hodges, and H. B. Dyson, "Calibration of power and energy meters for the far infrared/near millimeter spectral region," *Int. J. Infrared Millimeter Waves*, vol. 2, no. 4, 773–782, 1981.

[2]   Thomas Keating Ltd., Billingshurst, West Sussex, England.

[3]   C. C. Ling and G. M. Rebeiz, "A wideband monolithic submillimeter-wave quasi-optical power meter," in *IEEE Microwave Theory Tech. Soc. Int. Microwave Symp.*, May 1990, Dallas, TX.

[4]   D. B. Rutledge and S. E. Schwarz, "Planar multimode detector arrays for infrared and millimeter-wave applications," *IEEE J. Quantum Electron.*, vol. QE-17, Mar. 1981.

[5]   *American Institute of Physics Handbook*, 3rd ed. New York: McGraw-Hill, 1972.

[6]   G. M. Rebeiz, D. P. Kasilingam, Y. Guo, P. A. Stimson, and D. B. Rutledge, "Monolithic millimeter-wave two-dimensional horn imaging arrays," *IEEE Trans. Antennas Propagat.*, vol. 38, 1473–1482, Sept. 1990.

(a)

Loss component	loss, dB
Intrinsic pattern loss	0.2
Mismatch loss	2.2
Cross-polarization loss	0.2
Horn-to-horn coupling loss	0.1
Horn sidewall loss	0.7
Total calculated loss	3.4
Measured loss	3.6

(b)

Figure 1 Integrated-circuit horn array made by (a) anisotropic etching of silicon, and (b) the summary of measured and calculated losses reported by Rebeiz et al. [1]

APERTURE EFFICIENCY OF INTEGRATED-CIRCUIT HORN ANTENNAS

Yong Guo, Karen Lee, Philip Stimson, Kent Potter, and David Rutledge
Division of Engineering and Applied Science
California Institute of Technology
Pasadena, California 91125

ABSTRACT
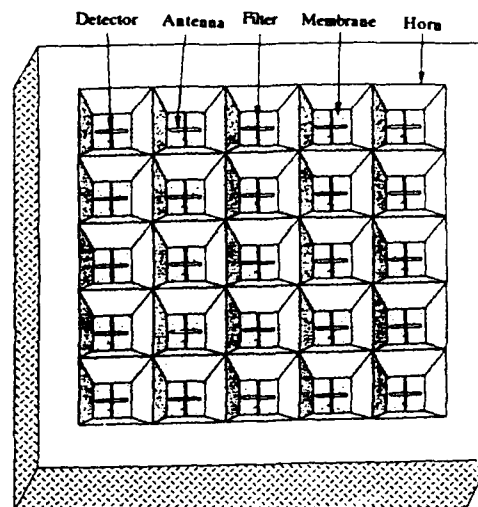We have improved the aperture efficiency of silicon integrated-circuit horn antennas by optimizing the length of the dipole probes and by coating the entire horn walls with gold. To make these measurements, we developed a new thin-film power-density meter for measuring power density with accuracies better than 5%. The measured aperture efficiency improved from 44% to 72% at 93 GHz. This is sufficient for use in many applications which now use machined waveguide horns.

INTRODUCTION

Rebeiz et al. [1] developed an integrated-circuit horn array based on anisotropic etching of silicon [Figure 1(a)]. The etch forms pyramidal cavities bounded by (111) crystal planes. Gold is evaporated on these walls to make them highly conducting. The power received by the horns is picked up by dipole probes suspended on 1-μm silicon-oxynitride membranes inside the horns. The power is detected by bismuth microbolometers. Horns were demonstrated at 242 and 93 GHz, and the technology appears to be quite suitable for scaling to the terahertz frequency range. These horns have several potential advantages for use in millimeter and sub-

millimeter arrays. The array is fully two-dimensional, and the horns are made simultaneously by integrated-circuit processing techniques. It should be possible to integrate superconducting tunnel-junction devices with the horns. An isotropic etching technology is also available in gallium arsenide, which suggests that it should be possible to make horns that would include monolithic Schottky diodes. The membranes appear fragile, but we have been able to mount beam lead diodes on them, and they have passed standard industrial temperature and vibration tests. However, the measured aperture efficiency was low; Rebeiz et al. reported a value of 44% at 93 GHz for an array with a period of $1\ \lambda$. This efficiency is not good enough for most applications.

Rebeiz' measured and calculated losses are summarized in Figure 1(b). The two major loss components are mismatch loss (2.2 dB) and horn-sidewall loss (0.7 dB). The mismatch loss was estimated from 7-GHz modeling experiments that indicated that the antenna impedance is $54 + j95\ \Omega$, compared with the bolometer resistance, $138\ \Omega$. The horn-sidewall loss arose from fact that the entire horn was not coated with gold; part was bare silicon with a resistivity of $0.5\ \Omega$ cm. The horn arrays are made as a stack of four wafers. One of these wafers includes the membranes; this wafer was not coated

with gold because the membranes would also have been covered over during the evaporation. The goal of this work was to eliminate these two sources of loss.

Another difficulty with the previous measurements was measuring the aperture efficiency. A 10% accuracy was claimed, but this is not adequate for testing antennas with higher efficiencies. Although the measurement is fundamentally only the ratio of received power to incident power density, there were many factors that complicated the measurement and affected the accuracy. The power density was calculated from the reading of a waveguide power meter connected by a calibrated directional coupler, together with the calculated gain of a standard gain horn. The received power was measured for a chopped signal, and this required an accurate knowledge of the effective value of the modulation waveform and the frequency roll-off of the bismuth microbolometer. To simplify the measurements and improve the accuracy, we developed a new thin-film power-density meter and used only four-wire DC electrical measurements in the calibration and measurement.

HORN FABRICATION

A range of horns with dipole probes varying in length from 0.32λ to 0.50λ were constructed. In addition, the horn walls on the membrane wafer were coated with gold by evaporating at an extreme angle so that the walls of the horns formed a shadow over the membrane. The bolometers were fabricated by a photoresist bridge technique [2]. They had resistances in the range 50 to 100 Ω, with typical resistance responsitivities of 20,000 Ω/W.

POWER-DENSITY METER

Recently there has been renewed interest in developing quasioptical power meters. Professor Derek Martin has recently developed an approach where the power is absorbed in a metallic thin film suspended in a closed gas cell [3]. The accuracy is reported to be 10%. Ling and Rebeiz are pursuing a design on a silicon-oxynitride film [4]. Our power meter (Figure 2) consists of an evaporated bismuth film with a sheet resistance of 189 Ω on a 4.5-μm-thick Mylar sheet. A film with this sheet resistance absorbs half the incident power and transmits half. The device is surrounded by a 5-cm-thick layer of styrofoam to reduce the convection heat loss and to block infrared radiation. The transmitted power is absorbed by a pyramidal beam dump lined with absorber. The power-density meter works as a bolometer. It absorbs power, heats up, and we measure the change in resistance by a four-wire measurement. The bolometer has an active area of 4 cm^2, and the typical resistance responsivity to RF radiation is 20 $\Omega/(W/cm^2)$. We have carefully considered and tested for different sources of error: resistance drift, edge effects, time constants, varying angle of incidence, and absorption in the styrofoam, and feel that the measurements are accurate to better than 5% for incident power densities greater than 100 $\mu W/cm^2$.

MEASUREMENTS

Both the power-density meter and the horn microbolometers were calibrated by a plot of the resistance R versus DC power P. This plot is of the form

$$R = R_0 + \Re P. \qquad (1)$$

where $\Re$ is the resistance responsivity in Ω/W. The resistance responsivity is calculated from the slope of the plot. There is
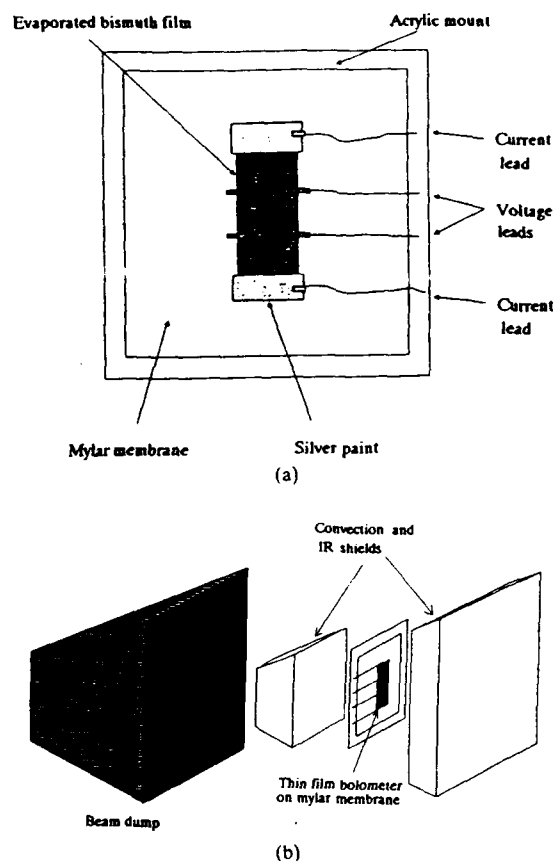
Figure 2 (a) Thin-film power-density meter and (b) assembly

one additional correction factor for the proportion of power that is absorbed by the power-density meter.

In the measurements, the signal source was a 93-GHz klystron with an output power of 170 mW feeding a horn 60 cm from the array. The resistance changes in the horn microbolometers were measured, and then the horn array was replaced by the power-density meter. The aperture efficiency η can then be written as a simple formula

$$\eta = \frac{A_m \Re_m \Delta R_h}{A_h \Re_h \Delta R_m}. \qquad (2)$$

where A_m is the area of the power-density meter, $\Re_m$ is the corrected resistance responsivity of the meter, ΔR_h is the resistance change of the horn microbolometer, A_h is area of the horn, R_h is the responsivity of the horn microbolometer, and ΔR_m is the resistance change of the power-density meter.

Figure 3(a) shows the measured efficiencies for different antenna lengths. Measurements were made first for membrane wafers without gold coating. After the membrane wafers were coated with gold, the efficiencies were measured again. The efficiency reaches its maximum value, 72%, for a length of 0.37 λ. For all but the longest probe, gold coating the walls of the membrane wafer improves the efficiency. The typical improvement is 6%. Figure 3(b) shows the estimated loss breakdown. The total calculated loss is 0.9 dB, compared with the measured value, 1.4 dB. There is still some mismatch

Figure 3 (a) Measured aperture efficiencies at 93 GHz versus antenna length. The efficiencies were measured before and after coating the membrane wafer with evaporated gold. (b) Summary of measured and calculated losses
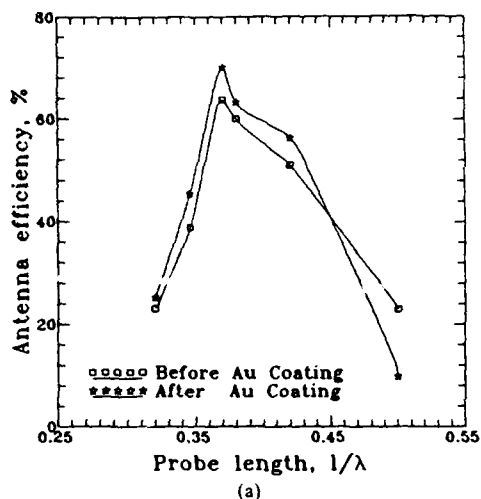
Loss component	loss, dB
Intrinsic pattern loss	0.2
Mismatch loss	0.4
Cross-polarization loss	0.2
Horn-to-horn coupling loss	0.1
Total calculated loss	0.9
Measured loss	1.4

(b)

loss (0.4 dB), because the bolometer resistance in the measurements was 90 Ω, compared with the resonant antenna resistance of 50 Ω that was measured on the microwave model. We also made a plot of efficiency for the frequency range from 77 to 109 GHz for antennas of various lengths, and this is shown in Figure 4. Probes with lengths in the range from 0.37
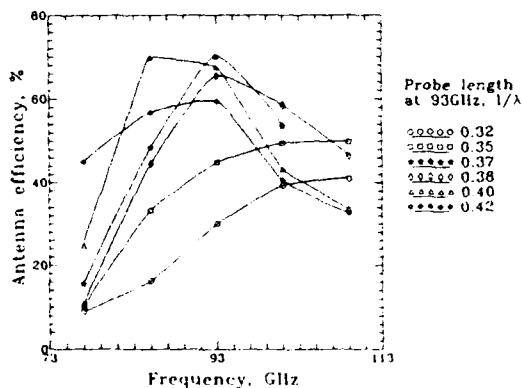
Figure 4 Aperture efficiency versus frequency for different dipole probe lengths
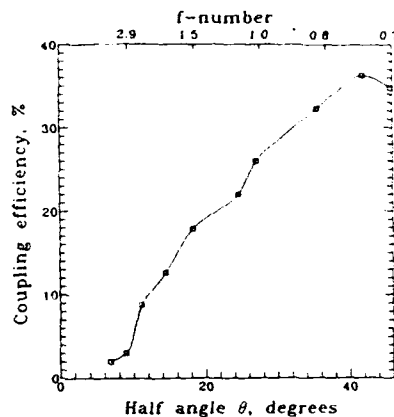
Figure 5 System coupling efficiency with a lens. The horizontal axis is the half angle subtended by the lens, which is varyied by changing stops in front of the lens

to 0.40 λ gave efficiencies better than 60%. The 3-dB bandwidths are of the order of 10 GHz.

Finally, we made measurements of the system coupling efficiency with a lens (Figure 5). This system coupling efficiency is the ratio of the detected power to the power incident on the lens. In the measurement, various stops were used to change the half angle subtended by a 100-mm-diameter lens with an f-number of 0.75. The highest system coupling efficiency with a lens is 36% for an f-number of 0.75. We estimate that the loss from reflection and absorption is the lens is 28%, so that it should be possible to achieve a coupling efficiency of 50% in a f-0.75 system with reflecting optics, compared with 24% reported by Rebeiz et al. [2].

CONCLUSION

We have improved the aperture efficiency of silicon integrated-circuit horn antennas by optimizing the length of the dipole probes and by coating the entire horn walls with gold. To make these measurements, we developed a new thin-film bolometer power-density meter for measuring power density with accuracies better than 5%. The measured aperture efficiency improved from 44% to 72% at 93 GHz. These horns are now efficient enough to be considered for use in remote sensing, plasma diagnostics, and radio astronomy.

REFERENCES

1 G M Rebeiz, D P Kasilingam, Y Guo, P A Stimson, D B Rutledge. "Monolithic Millimeter-Wave Two-Dimensional Horn Imaging Arrays," IEEE Trans. Antennas Propagat., to be published

2 D P Neikirk, W W Lam, and D B Rutledge. "Far-Infrared Microbolometer Detectors," Int J Infrared Millimeter Waves, Vol 5, 1984, pp 245-278 The bridge technique described in this

paper uses a CF$_4$ plasma to make a buffer layer for the bridge. We are currently using a thin layer of aluminum as the buffer layer.

3. Professor Martin's power meter is now commercially available from Thomas Keating Ltd., Billinghurst, West Sussex, England.
4. C. C. Ling and G. M. Rebeiz, "A Wide-Band Monolithic Submillimeter-Wave Quasi-Optical Power Meter," IEEE MTT-S International Microwave Symposium, May, 1990, Dallas, Texas.

Received 4-30-90

DISTRIBUTION LIST

addresses	number of copies
RL/ERAA ATTN: JOHN P. TURTLE Hanscom AFB MA 01731-5000	10
CALIFORNIA INSTITUTE OF TECHNOLOGY DEPT OF ELECTRICAL ENGINEERING 116-81 PASADENA, CA 91124	5
PL/SUL Technical Library Griffiss AFB NY 13441-5700	1
Administrator Defense Technical Info Center DTIC-FDAC Cameron Station Building 5 Alexandria VA 22304-6145	2
Strategic Defense Initiative Office Office of the Secretary of Defense Wash DC 20301-7100	2
HQ USAF/SCTT Washington DC 20330-5190	1
SAF/AQSC Pentagon Rm 4D 269 Wash DC 20330	1
Naval Warfare Assessment Center GIDEP Operations Center/Code QA-50 ATTN: E Richards Corona CA 91718-5000	1

HQ AFSC/XTH   1
Andrews AFB MD 20334-5000

HQ SAC/SCPT   2
OFFUTT AFB NE 65046

HQ TAC/DRIY   1
ATTN: Maj. Divine
Langley AFB VA 23665-5575

HQ TAC/XP-JSG   1
Langley AFB VA 23665-5520

Weapons Laboratory/NTAAB   1
ATTN: Dr. Carl E. Baum
Kirtland AFB NM 87117-6008

                                                              .

ASD/ENEMS   1
Wright-Patterson AFB OH 45433-6503

WRDC/AAAI-4   1
Wright-Patterson AFB OH 45433-6543

WRDC/AAAI-2   .   1
ATTN: Mr Franklin Hutson
WPAFB OH 45433-6543

AFIT/LDEE   1
Building 642, Area B
Wright-Patterson AFB OH 45433-6583

WRDC/MLPO   1
ATTN: D.L. Denison
WPAFB OH 45433-6533

WRDC/MTEL   1
Wright-Patterson AFB OH 45433

AUL/LSE   1
Blg
Maxwell AFB AL 36112-5564

HQ ATC/TTOI   1
ATTN: Lt Col Killian
Randolph AFB TX 78150-5001

US Army Strategic Def   1
CSSD-IM-PA
PO Box 1500
Huntsville AL 35807-3801

Commanding Officer   1
Naval Avionics Center
Library D/765
Indianapolis IN 46219-2189

Commanding Officer   1
Naval Ocean Systems Center
Technical Library
Code 96423
San Diego CA 92152-5000

Cmdr   1
Naval Weapons Center
Technical Library/C3431
China Lake CA 93555-6001

Superintendent   1
Code 524
Naval Postgraduate School
Monterey CA 93943-5000

Space & Naval Warfare Systems Comm   1
Washington DC 20363-5100

CDR, U.S. Army Missile Command   2
Redstone Scientific Info Center
AMSMI-RD-CS-R/ILL Documents
Redstone Arsenal AL 35898-5241

Advisory Group on Electron Devices   2
Attn: Documents
2011 Crystal Drive,Suite 307
Arlington VA 22202

Los Alamos National Laboratory   1
Report Library
MS 5000
Los Alamos NM 87544

Commander/USAISC   1
ATTN: ASOP-DO-TL
Bldg 61801
Ft Huachuca AZ 85613-5000

DOT Library/10A Section   1
M-493.2
800 Independence Ave, S.W.
Wash DC 20591

1839 EIG/EIX   1
Keesler AFB MS 39534-6348

AFEWC/ESRI   3
San Antonio TX 78243-5000

Software Engineering Inst (SEI)   1
Technical Library
5000 ForbesAve
Pittsburgh PA 15213

Director NSA/CSS   1
W157
9800 Savage Road
Fort Meade MD 21055-6000

NSA   1
ATTN: D. Alley
Div X911
9800 Savage Road
Ft Meade MD 20755-6000

Director   1
NSA/CSS P12
ATTN: Mr. Dennis Heinbuch
9800 Savage Road
Fort George G. Meade MD 20755-6000

DoD   1
P31
9800 Savage Road
Ft. Meade MD 20755-6000

DIRNSA   1
R509
9800 Savage Road
Ft Meade MD 20775

NSA/CSS   1
R9
Fort George G. Meade MD 20755-6000

Director   1
NSA/CSS
R09/R & E BLDG
Fort George G. Meade MD 20755-6000

DOD Computer Center   1
C/TIC
9800 Savage Road
Fort George G. Meade MD 20755-6000

Defense Technology Sec Admin (DTSA)   1
ATTN: STTD/Patrick Sullivan
400 Army Navy Drive
Suite 300
Arlington VA 22202

Dr. Andrew Smith   1
Applied Technology Division
TRW Space and Technology Group
One Space Park
Redondo Beach, CA 90278

Dr. Robert A. Buhrman   1
Dept of Applied & Engineering Phy.
Cornell University
Ithaca, NY 14853

                                                       1

Dr. John X. Przybysz
Westinghouse Science & Tech. Cen.
1310 Beulah Road
Pittsburg, PA 15235

Dr. Richard Ralston   1
Analog Device Technology Group
MIT Lincoln Laboratory
Lexington, MA 02173-0073

                                                       1

Dr. Harold Weinstock
AFOSR/NE
Bolling AFB, DC 20332-6448

Prof. Malcolm Beasley   1
Dept. of Applied Physics
Edward L. Ginzton Laboratory
Stanford University
Stanford, CA 94305

Dr. Ted Van Duzer   1
Dept of Electronics Engineering
  and Computer Science
University of California
Berkeley, CA 94720

Dr. James Lukens   1
Dept. of Physics
State University of New York
Stony Brook, NY 11794-3800

Dr. Elie K. Track   1
HYPRES Inc.
500 Executive Blvd.
Elmsford, NY 10523

Dr. Martin Nisenoff   1
Code 6854
Naval Research Laboratory
Washington, DC 20375-5000

Prof. David Rutledge   1
California Institute of Technology
Mail Code 116-81
Pasadena, CA 91125

Dr. Stanley Feible   1
Micrilor Inc.
17 Lakeside Office Park
North Avenue
Wakefield, MA 01880

Dr. Margaret Frerking   1
MS 168-314
Jet Propulsion Laboratory
4300 Oak Grove Dr.
Pasadena, CA 91109

Dr. Henry Leduc   1
MS 122-123
Jet Propulsion Laboratory
4800 Oak Grove Dr.
Pasadena, CA 91109

Prof. Thomas Phillips   1
MS 320-47
California Institute of Technology
Pasadena, CA 91125

Prof. Robert Mattauch   1
Dept. of Electrical Engineering
University of Virginia
Charlottesville, VA 22901

Dr. Frank Patton   1
DARPA/DSO
3701 North Fairfax Drive
Arlington, VA 22203-1714

Dr. William McGrath   1
MS 168-314
Jet Propulsion Laboratory
4800 Oak Grove Dr.
Pasadena, CA 91109

Prof. Neal Erickson   1
Dept. of Physics and Astronomy
Univ. of Massachusetts
Amherst, MA 01002

Prof. Paul Richards   1
Dept. of Physics
University of California
Berkeley, CA 94720

Prof. Marc Feldman   1
Dept. of Electrical Engineering
University of Rochester
Rochester, NY 14623

Dr. A. R. Kerr   1
National Radio Astronomy Obser.
2015 Ivy Rd.
Charlottesville, VA 22903-1797

Dr. Robin Harvey   1
Hughes Research Laboratory
3011 S. Malibu Canyon Rd.
Malibu, CA 90265

Dr. Fernand D. Bedard   1
NSA Attn. R53
9300 Savage Rd.
Fort George G. Meade, VA 20755-6000

Department of Defense   1
SDIO/TNI
Washington, DC 20301-7100

Dr. Bruce Murdock   1
Superconductive Systems
Tektronic Laboratories
P.O. Box 500, Mail Sta. 50-324
Beaverton, OR 97077

Dr. James W. Mink, Director   1
Electronics Division
U.S Army Research Office
P.O. Box 12211
Research Triangle Park, NC 27709

Prof. Gabriel Rebeiz   1
Elect. Eng. and Computer Science
    Department
University of Michigan
Ann Arbor, MI 48102-2122

Prof. Michael Wengler   1
Department of Electrical Eng.
University of Rochester
Rochester, NY 14627

Dr. Richard Withers   1
Conductus, Inc.
969 West Maude Ave
Sunnyvale, CA 94055

Dr. Charles T. Byvik   1
W. J. Schafer Assoc.
1901 N. Fort Myer Drive
Suite 800
Arlington, VA 22209

Dr. Richard Harris   1
NIST
Dept. of Commerce
325 Broadway
Boulder, CO 80303

MISSION

OF

ROME LABORATORY

Rome Laboratory plans and executes an interdisciplinary program in research, development, test, and technology transition in support of Air Force Command, Control, Communications and Intelligence (C^3I) activities for all Air Force platforms. It also executes selected acquisition programs in several areas of expertise. Technical and engineering support within areas of competence is provided to ESD Program Offices (POs) and other ESD elements to perform effective acquisition of C^3I systems. In addition, Rome Laboratory's technology supports other AFSC Product Divisions, the Air Force user community, and other DOD and non-DOD agencies. Rome Laboratory maintains technical competence and research programs in areas including, but not limited to, communications, command and control, battle management, intelligence information processing, computational sciences and software producibility, wide area surveillance/sensors, signal processing, solid state sciences, photonics, electromagnetic technology, superconductivity, and electronic reliability/maintainability and testability.